

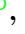



# $\Delta$ -baryon axialvector and pseudoscalar form factors, and associated PCAC relations

Pei-Lin Yin<sup>1</sup> , Chen Chen<sup>2,3</sup> ,  
Christian S. Fischer<sup>4,5</sup> , Craig D. Roberts<sup>6,7</sup> 

<sup>1</sup>College of Science, Nanjing University of Posts and Telecommunications, Nanjing 210023, China

<sup>2</sup>Interdisciplinary Center for Theoretical Study, University of Science and Technology of China, Hefei, Anhui 230026, China

<sup>3</sup>Peng Huanwu Center for Fundamental Theory, Hefei, Anhui 230026, China

<sup>4</sup>Institut für Theoretische Physik, Justus-Liebig-Universität Gießen, D-35392 Gießen, Germany

<sup>5</sup>Helmholtz Forschungsakademie Hessen für FAIR (HFHF), GSI Helmholtzzentrum für Schwerionenforschung,  
Campus Gießen, 35392 Gießen, Germany

<sup>6</sup>School of Physics, Nanjing University, Nanjing, Jiangsu 210093, China

<sup>7</sup>Institute for Nonperturbative Physics, Nanjing University, Nanjing, Jiangsu 210093, China

Email: chenchen1031@ustc.edu.cn (C. Chen); cdroberts@nju.edu.cn (C. D. Roberts).

2023 May 16

**Abstract** A quark+diquark Faddeev equation treatment of the baryon bound state problem in Poincaré-invariant quantum field theory is used to deliver parameter-free predictions for all six  $\Delta$ -baryon elastic weak form factors. Amongst the results, it is worth highlighting that there are two distinct classes of such  $\Delta$ -baryon form factors,  $(g_1, g_3, G_{\pi\Delta\Delta})$ ,  $(h_1, h_3, H_{\pi\Delta\Delta})$ , the functions within each of which are separately linked via partial conservation of axial current (PCAC) and Goldberger-Treiman (GT) relations. Respectively within each class, the listed form factors possess qualitatively the same structural features as the nucleon axial, induced pseudoscalar, and pion-nucleon coupling form factors. For instance, the  $\Delta$ -baryon  $g_1$  axial form factor can reliably be approximated by a dipole function, characterised by an axial charge  $g_A^{\Delta^+} = 0.71(9)$  and mass-scale  $m_A^{\Delta^+} = 0.95(2)m_{\Delta}$ . Moreover, the two distinct  $\Delta$ -baryon PCAC form factor relations are satisfied to a high degree of accuracy on a large range of  $Q^2$ ; the associated GT relations present good approximations only on  $Q^2/m_{\Delta}^2 \simeq 0$ ; and pion pole dominance approximations are reliable within both classes. There are two  $\pi\Delta\Delta$  couplings:  $g_{\pi\Delta\Delta} = 10.46(1.88)$ ;  $h_{\pi\Delta\Delta} = 35.73(3.75)$ ; and the associated form factors are soft. Such couplings commonly arise in phenomenology, which may therefore benefit from our analyses. A flavour decomposition of the axial charges reveals that quarks carry 71% of the  $\Delta$ -baryon spin. The analogous result for the proton is  $\approx 65\%$ .

## 1 Introduction

The response of baryons to electromagnetic probes is much studied, both experimentally [1–9] and theoretically [10–12]. An entirely new perspective on baryon structure is provided by weak-interaction probes, with form factors that can be measured in, *e.g.*, neutrino-nucleus scattering. Here, nucleon axialvector and pseudoscalar form factors are the archetypes, being crucial inputs for Standard Model tests via weak interactions, neutrino-nucleus scattering and parity violation exper-

iments. Consequently, a diverse array of theory tools – using both continuum [13–16] and lattice [17–19] formulations of hadron bound state problems – has recently been employed to deliver a better understanding of their behaviour.

The lightest excitations of the nucleon are the  $\Delta(1232)$ -baryons. Theoretically, as  $(I, J^P) = (\frac{3}{2}, \frac{3}{2}^+)$  systems,  $\Delta$ -baryons are less complex than  $(\frac{1}{2}, \frac{1}{2}^+)$  nucleons because their Poincaré-covariant wave functions are simpler. For instance, viewed from a modern quark + diquark perspective [20],  $\Delta$ -baryons only contain isovector-axialvector diquark correlations [21], whereas isoscalar-scalar diquarks also play a large role in nucleons. Such structural distinctions make comparisons between predictions for nucleon and  $\Delta$ -baryon properties useful in developing an understanding of how quantum chromodynamics (QCD) produces systems constituted from three valence quarks. These features explain why much theoretical attention has been devoted to the calculation of  $\Delta$ -baryon elastic electromagnetic form factors [22–29], even though measurement of such form factors is impossible because of the very short lifetime of these resonances:  $\tau_{\Delta} \approx 10^{-26}\tau_n$ , where  $\tau_n$  is the lifetime of a free neutron. (Estimates of  $\Delta$ -baryon magnetic moments have been produced through analyses of  $\pi^+p \rightarrow \pi^+p\gamma$  reactions [30, RPP].)

Against this backdrop, it is natural to develop comparative studies of the weak-interaction structure of the nucleon and  $\Delta$ -baryon. As well as being interesting in their own right, predictions for such quantities as the  $\Delta$ -baryon axial charge,  $g_A^{\Delta}$ , and  $\pi\Delta\Delta$  coupling, unified with analogous nucleon properties, can provide valuable inputs (constraints) for effective field theories em-

ployed in low-energy hadron physics [31, 32]. The calculation of  $\Delta$ -baryon elastic weak-interaction form factors is also a useful preliminary to delivering reliable predictions for the weak-probe induced  $N \rightarrow \Delta$  transition, whose form factors are experimentally accessible and which may play an important role in understanding long-baseline and atmospheric neutrino-nucleus scattering experiments [33–36].

It is thus unsurprising that numerous analyses have computed values for  $g_A^\Delta$  and  $g_{\pi\Delta\Delta}$  – see, *e.g.*, Refs. [37–50]. Amongst them, however, only one pair of studies [40, 41], working with lattice-regularised QCD (lQCD), has provided results for the entire set of four-plus-two form factors required to completely describe  $\Delta$ -baryon axial and pseudoscalar currents. Unfortunately, those calculations were performed with unphysically large pion masses and the results possess significant uncertainties. A chiral quark-soliton model ( $\chi$ QSM) has been used to compute the four axial form factors [50].

Continuum Schwinger function methods (CSMs) provide an alternative to models and lQCD computations in hadron physics. In such applications, contemporary progress and challenges are canvassed elsewhere [10–12, 51?–55]. Of particular relevance herein is the recent construction and use [14–16] of symmetry-preserving axial and pseudoscalar currents appropriate for baryons described by the fully-interacting quark+nonpointlike-diquark Faddeev equation introduced in Refs. [56–58]. This has enabled the use of CSMs to complete a parameter-free comparative study and unification of the weak-interaction structure of the nucleon and  $\Delta$ -baryon. At the simplest level, the outcomes can be used to test the current construction via comparisons with results from models and lQCD. Passing such tests, sound predictions for weak  $N \rightarrow \Delta$  transitions can follow. Such predictions can be tested because, *e.g.*, data exist [59, 60] from which the axial  $\pi N \rightarrow \Delta$  transition form factor may be extracted after extending existing reaction models [61].

Our discussion is organised as follows. Section 2.1 explains the structure of the  $\Delta$ -baryon elastic matrix elements of the axialvector and pseudoscalar currents and introduces the full array of associated form factors. The quark+diquark Faddeev equation used to describe the  $\Delta$ -baryon is sketched in Sec. 3 along with the related symmetry preserving current. Our results are presented in Sec. 4, wherein they are also compared with those from other studies, and followed in Sec. 5 with a brief discussion of the flavour-separated  $\Delta$ -baryon axial charges and the quark contribution to their total spin. Section 6 contains a summary and perspective. Numerous technical details are collected in appendices.

## 2 $\Delta(1232)$ axial and pseudoscalar currents

### 2.1 General structure

Introducing the column vector  $\psi = (u, d)^T$ , where  $u, d$  are quark fields, the axialvector current operator can be written  $\mathcal{A}_{5\mu}^j(x) = \bar{\psi}(x) \frac{\tau^j}{2} \gamma_5 \gamma_\mu \psi(x)$ , where the isospin (flavour) structure is given by the Pauli matrices,  $\{\tau^i | i = 1, 2, 3\}$ , with  $\tau^3$  representing the neutral current and  $\tau^{1\pm i2} := (\tau^1 \pm i\tau^2)/2$  expressing the charged currents. The in- $\Delta$  expectation value of this operator is [40, 41]:

$$\mathcal{J}_{5\mu}(K, Q) := \langle \Delta(P_f; s_f) | \mathcal{A}_{5\mu}^j(0) | \Delta(P_i; s_i) \rangle \quad (1a)$$

$$= \bar{u}_\alpha(P_f; s_f) \Gamma_{5\mu, \alpha\beta}(Q) u_\beta(P_i; s_i), \quad (1b)$$

where  $P_i(s_i)$  and  $P_f(s_f)$  are  $\Delta$ -baryon incoming and outgoing momenta (spins), with  $P_f^2 = -m_\Delta^2 = P_i^2$ ; and  $K = (P_f + P_i)/2$  is the average momentum and  $Q = P_f - P_i$  is the momentum of the weak probe. In writing Eq. (1b), we have used a Euclidean space Rarita-Schwinger spinor, which is the same for all  $\Delta$ -baryons and whose properties are explained elsewhere [28, Appendix B]. Notably, the choice of  $j$  constrains the initial and final charge-states of the  $\Delta$ -baryon, *e.g.*,  $j = 3$  entails that they are both the same.

The  $\Delta$ -baryon axial current vertex in Eq. (1b) has the general form:

$$\Gamma_{5\mu, \alpha\beta}(Q) = -\frac{1}{2} \gamma_5 \left[ \delta_{\alpha\beta} \left( g_1(Q^2) \gamma_\mu + i g_3(Q^2) \frac{Q_\mu}{2m_\Delta} \right) - \frac{Q_\alpha Q_\beta}{4m_\Delta^2} \left( h_1(Q^2) \gamma_\mu + i h_3(Q^2) \frac{Q_\mu}{2m_\Delta} \right) \right], \quad (2)$$

where  $g_1, g_3, h_1, h_3$  are four Poincaré invariant form factors.

The matrix element of the analogous pseudoscalar operator,  $\mathcal{P}_5^j(x)$ , is

$$\mathcal{J}_5(K, Q) := \bar{u}_\alpha(P_f; s_f) \Gamma_{5, \alpha\beta}(Q) u_\beta(P_i; s_i), \quad (3)$$

with

$$\Gamma_{5, \alpha\beta}(Q) = -\frac{1}{2} \gamma_5 \left[ \delta_{\alpha\beta} \tilde{g}(Q^2) - \frac{Q_\alpha Q_\beta}{4m_\Delta^2} \tilde{h}(Q^2) \right], \quad (4)$$

where  $\tilde{g}$  and  $\tilde{h}$  are the two Poincaré invariant pseudoscalar form factors.

Hereafter we assume isospin symmetry and, unless otherwise noted, choose  $j = 3$ . The elastic weak form factors of the other  $\Delta$ -baryons in the multiplet can be obtained following the rules detailed in Appendix A.

In practice, it is useful to sum over initial- and final-state spins in order to remove the spinors in the given

current:

$$J_{5(\mu),\lambda\omega}(K, Q) := \sum_{s_f, s_i} u_\lambda(P_f; s_f) \mathcal{J}_{5(\mu)}(K, Q) \bar{u}_\omega(P_i; s_i) \quad (5a)$$

$$= \Lambda_+(P_f) R_{\lambda\alpha}(P_f) \Gamma_{5(\mu),\alpha\beta}(Q) \Lambda_+(P_i) R_{\beta\omega}(P_i), \quad (5b)$$

where the positive-energy spinor projector and Rarita-Schwinger projection operator are, respectively:

$$\Lambda_+(P) = \frac{1}{2} \left( \mathbb{I}_D + \gamma \cdot \hat{P} \right), \quad (6a)$$

$$R_{\mu\nu}(P) = \delta_{\mu\nu} \mathbb{I}_D - \frac{1}{3} \gamma_\mu \gamma_\nu + \frac{2}{3} \hat{P}_\mu \hat{P}_\nu \mathbb{I}_D - \frac{i}{3} [\hat{P}_\mu \gamma_\nu - \hat{P}_\nu \gamma_\mu], \quad (6b)$$

with  $\hat{P}_\mu = P_\mu / (im_\Delta)$ . Using Eq. (5), one obtains the desired form factors by sensibly chosen matrix projection operations – see Appendix B.

## 2.2 PCAC and Goldberger-Treiman relations

Using Ward-Green-Takahashi identities, one can obtain the following partially conserved axial-vector current (PCAC) relation between the current operators:

$$\partial_\mu \mathcal{A}_{5\mu}^j(x) + 2m_q \mathcal{P}_5^j(x) = 0. \quad (7)$$

Evaluating the expectation value of this current, one obtains the  $\Delta$ -baryon PCAC relation:

$$Q_\mu J_{5\mu,\lambda\omega}(K, Q) + 2im_q J_{5,\lambda\omega}(K, Q) = 0, \quad (8)$$

which entails

$$\begin{aligned} & \delta_{\alpha\beta} \left( g_1 - \frac{Q^2}{4m_\Delta^2} g_3 \right) - \frac{Q_\alpha Q_\beta}{4m_\Delta^2} \left( h_1 - \frac{Q^2}{4m_\Delta^2} h_3 \right) \\ &= \frac{m_q}{m_\Delta} \left( \delta_{\alpha\beta} \tilde{g} - \frac{Q_\alpha Q_\beta}{4m_\Delta^2} \tilde{h} \right). \end{aligned} \quad (9)$$

Considering the diagonal ( $\alpha = \beta$ ) and non-diagonal ( $\alpha \neq \beta$ ) components of Eq. (9) separately, one finds the following two independent PCAC relations at the form factor level [41]:

$$g_1 - \frac{Q^2}{4m_\Delta^2} g_3 = \frac{m_q}{m_\Delta} \tilde{g}, \quad (10a)$$

$$h_1 - \frac{Q^2}{4m_\Delta^2} h_3 = \frac{m_q}{m_\Delta} \tilde{h}. \quad (10b)$$

Notably, Eqs. (10) are consequences of the operator relation, Eq. (7). So, only results that comply with these identities can be called realistic; and no tuning of any element in a given calculation may be employed to secure these outcomes.

Expanding on the nucleon case [15, 62], one may define two  $\pi$ - $\Delta$  form factors,  $G_{\pi\Delta\Delta}$ ,  $H_{\pi\Delta\Delta}$ :

$$\tilde{g}(Q^2) =: \frac{m_\pi^2}{Q^2 + m_\pi^2} \frac{f_\pi}{m_q} G_{\pi\Delta\Delta}(Q^2), \quad (11a)$$

$$\tilde{h}(Q^2) =: \frac{m_\pi^2}{Q^2 + m_\pi^2} \frac{f_\pi}{m_q} H_{\pi\Delta\Delta}(Q^2), \quad (11b)$$

where  $f_\pi \approx 92$  MeV is the pion leptonic decay constant. At the pion mass pole,  $Q^2 + m_\pi^2 = 0$ , the residues of  $\tilde{g}$  and  $\tilde{h}$  define two  $\pi$ - $\Delta$  coupling constants:

$$G_{\pi\Delta\Delta}(-m_\pi^2) =: g_{\pi\Delta\Delta}, \quad H_{\pi\Delta\Delta}(-m_\pi^2) =: h_{\pi\Delta\Delta}. \quad (12)$$

In systematic analyses of low-energy phenomena,  $g_{\pi\Delta\Delta}$  and  $h_{\pi\Delta\Delta}$  should relate the fields of the  $\pi$  and  $\Delta$  in two different ways. Using the currents, Eqs. (1) – (4), the PCAC relations, Eqs. (10), and analyticity of  $g_3$ ,  $h_3$  in the neighbourhood of the pion pole, one immediately obtains two Goldberger-Treiman (GT) relations for the  $\Delta$ -baryon:

$$g_1(0) = \frac{f_\pi}{m_\Delta} G_{\pi\Delta\Delta}(0), \quad (13a)$$

$$h_1(0) = \frac{f_\pi}{m_\Delta} H_{\pi\Delta\Delta}(0). \quad (13b)$$

It is now apparent that the four axial and two pseudoscalar form factors can be divided into two classes:  $\{g_1, g_3, \tilde{g}\}$  and  $\{h_1, h_3, \tilde{h}\}$ . Each class has its own, independent PCAC and GT relations. Comparing with the nucleon,  $g_1$ ,  $h_1$  are kindred to the nucleon axial-vector form factor  $G_A$ ;  $g_3$ ,  $h_3$  are analogous to the induced-pseudoscalar form factor,  $G_P$ ; and  $\tilde{g}$ ,  $\tilde{h}$  are akin to the pseudoscalar form factor,  $G_5$ .

## 3 $\Delta(1232)$ Faddeev equation framework

Herein, we treat the baryon bound-state problem using a Poincaré-covariant quark+diquark Faddeev equation, which is sketched in Fig. 1. Crucially, the diquark correlations are nonpointlike and fully interacting; consequently, *inter alia*, Fermi statistics are properly expressed. As explained elsewhere [10, 20], the approach has been used widely with success. Furthermore, to meet our goal of unifying nucleon and  $\Delta$ -baryon electroweak properties, we use precisely the formulation employed in Refs. [14–16]. This ‘‘QCD-kindred’’ approach is detailed, *e.g.*, in Ref. [15, Appendix A]. Nevertheless, so as to make this presentation self-contained, we reiterate some of that material in Appendix C, introducing  $\Delta$ -baryon specific statements in place of such for the nucleon.

Regarding  $I = \frac{3}{2}$   $\Delta$ -baryons, two types of diquark correlations may be present: isovector-axialvector; and

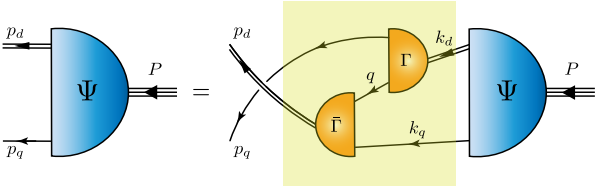


**Fig. 1** Quark+di-quark Faddeev equation. The solution,  $\Psi$ , is the Poincaré-covariant, matrix-valued Faddeev amplitude for a baryon with total momentum  $P = p_q + p_d = k_q + k_d$  constituted from three valence quarks, two of which are always contained in a nonpointlike diquark correlation.  $\Psi$  expresses the relative momentum correlation between the dressed-quarks and -diquarks. Legend. *Shaded rectangle* – Faddeev kernel; *single line* – dressed-quark propagator,  $S$ ;  $\Gamma$  – diquark correlation amplitude; and *double line* – diquark propagator,  $\mathcal{D}$ . (See Appendix C for specification of these functions.) Regarding ground-state  $\Delta$ -baryons, only isovector-axialvector diquarks ( $\{dd\}$ ,  $\{ud\}$ ,  $\{uu\}$ ) play a material role [21].

isovector-vector. However, detailed analyses reveal [21] that isovector-vector diquarks may be neglected with practically no cost. Hence, we work with the simple isovector-axialvector Faddeev amplitude detailed in Appendix C.3. These diquarks are characterised by the following mass-scale (in GeV):

$$m_{\{uu\}_{1+}} = m_{\{ud\}_{1+}} = m_{\{dd\}_{1+}} = 0.89, \quad (14)$$

whose value has been constrained by successful applications to many baryons – see, *e.g.*, Refs. [63–67].

Six distinct contributions are required to provide a symmetry-preserving treatment of the axialvector and pseudoscalar currents of a baryon described by the Faddeev equation in Fig. 1 [14, 15]. For  $\Delta$ -baryons constituted solely from axialvector diquarks, however, Diagram (3) does not contribute because there are no other participating diquarks into which the axialvector can be transformed. Mathematical realisations of the images in Fig. 2 are provided in Appendix D.

## 4 Results and discussion

### 4.1 Axial-vector form factors

Our predictions for  $g_1(x)$ ,  $g_3(x)$ ,  $x = Q^2/m_\Delta^2$ , are depicted in Fig. 3, together with results from IQCD [41] and a  $\chi$ QSM [50]. As described in Sec. 2.1,  $g_1(x)$  and  $g_3(x)$  are analogues of the nucleon axial and induced pseudoscalar form factors,  $G_A(x)$ ,  $G_P(x)$ , respectively. Here and hereafter, each of our predictions is embedded in a band that expresses the impact of a  $\pm 5\%$  variation in the axialvector diquark mass and, consequently, the width of its correlation amplitude, Eq. (C.26).

Considering Fig 3A, one sees that our CSM prediction agrees qualitatively with the IQCD results. One

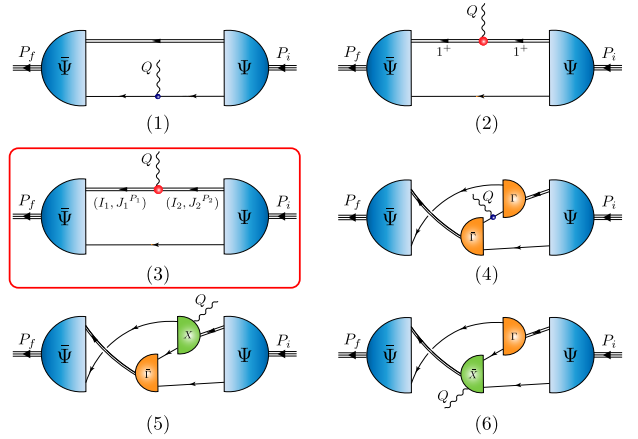


**Fig. 2** Axial or pseudoscalar current that ensures PCAC for on-shell baryons described by a Faddeev amplitude produced by the equation depicted in Fig. 1. Legend. *Single line*, dressed-quark propagator; *undulating line*, the axialvector or pseudoscalar current;  $\Gamma$ , diquark correlation amplitude; *double line*, diquark propagator; and  $\chi$ , seagull terms. For  $\Delta$ -baryons, Diagram (3) does not contribute.

cannot say more because the IQCD uncertainties are too large. Considering the  $\chi$ QSM result [50], which is the only other available calculation of  $\Delta(1232)$ -baryon axialvector form factors, there is agreement at low- $x$ , but the  $\chi$ QSM produces a softer  $x$ -dependence. Given that the CSM framework is explicitly Poincaré-covariant, one may reasonably expect its form factor predictions to remain reliable as  $x$  increases, whereas those obtained in formulations which lack this feature are likely to degrade.

On the domain depicted, the central CSM result is accurately interpolated using Eq. (E.53) with the coefficients in Table 2. Interestingly,  $g_1(x)$  can be interpolated, almost equally well, by a dipole form

$$g_1(x) = \frac{g_1(0)}{(1 + x/(m_A^\Delta/m_\Delta)^2)^2}, \quad (15)$$

with the axial mass  $m_A^\Delta = 0.95(2)m_\Delta$ . In this context, the nucleon axial mass is  $m_A = 1.23(3)m_N$ , where  $m_N$  is the nucleon mass. Evidently, converted to GeV, these dipole masses are equal within mutual uncertainties.

The  $\Delta$ -baryon axial charge is defined via  $g_A^\Delta = g_1(x = 0)$ ; and although predictions for  $\Delta$ -baryon axial form factors are rare, there are many calculations of  $g_A^\Delta$ , using a variety of frameworks. In Fig. 4, we depict our predictions:

$$g_A^{\Delta^+} = 0.71(9), \quad g_A^{\Delta^{++}} = 2.13(27) = 3g_A^{\Delta^+}, \quad (16)$$

along with values obtained using other methods. Evidently, there is general agreement on the results, although the IQCD values lie systematically lower than other estimates.

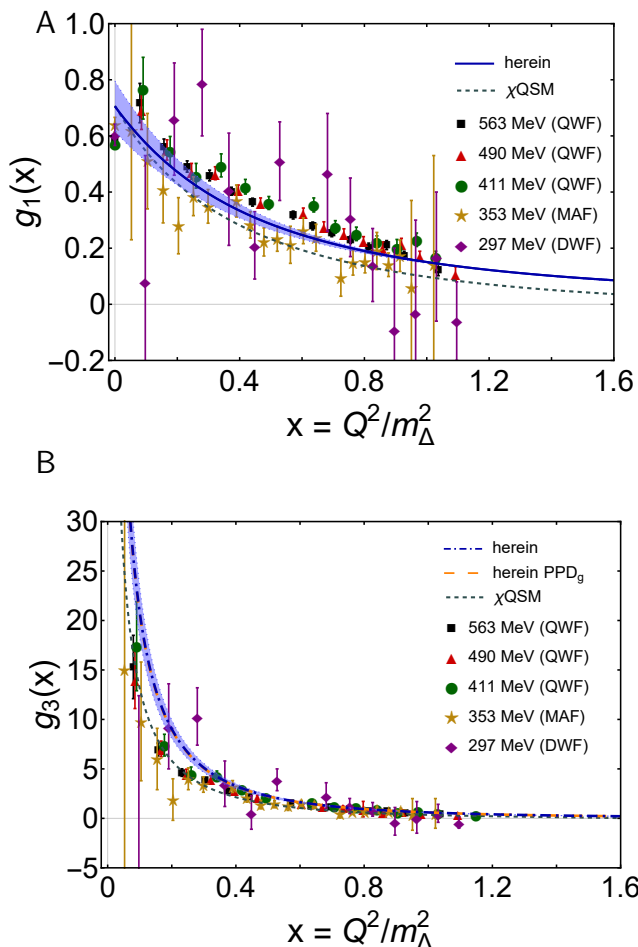


**Fig. 3** Panel A.  $g_1(x)$  calculated herein – blue curve within lighter blue uncertainty band. Panel B.  $g_3(x)$  calculated herein – dot-dashed blue curve within lighter blue uncertainty band; and long-dashed orange curve – PPD approximation, Eq. (17), employing our CSM result for  $g_1(x)$ . Comparisons in both panels: IQCD [41] – quenched (QWF) [black squares –  $m_\pi = 563$  MeV, red triangles –  $m_\pi = 490$  MeV, green circles –  $m_\pi = 411$  MeV], mixed (MAF) [gold stars –  $m_\pi = 353$  MeV], domain wall (DWF) [purple diamonds –  $m_\pi = 297$  MeV]; and  $\chi$ QSM [50] – short-dashed gray curve.

In Table 1, referring to Fig. 2, we list the relative strengths of each diagram contribution to  $g_A^{\Delta^+}$ . Diagram (1), with the weak boson striking the dressed quark in association with a spectator axialvector diquark, is dominant. On the other hand, Diagrams (2) and (4), both contribute materially. There is no contribution from Diagrams (5) and (6) because the seagull terms, Eqs. (D.50a), (D.50c), are purely longitudinal; hence, cannot contribute to  $g_1$ , which is entirely determined by the  $Q$ -transverse part of the  $\Delta$ -baryon axial current – see the  $g_1$  projection, Eqs. (B.15) – (B.17).

Our prediction for  $g_3(x)$  is drawn in Fig 3B and compared with results from IQCD and a  $\chi$ QSM. Interpolation of our central result is obtained using Eq. (E.54) with the coefficients in Table 2. Once again, given the

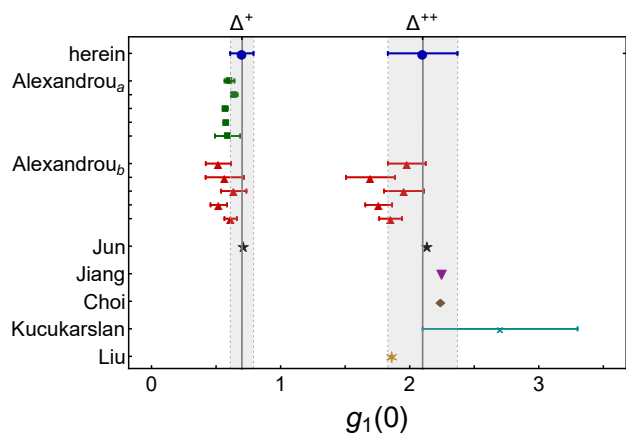


**Fig. 4** Our predictions for  $g_1(0)$  of the  $\Delta^+$  and  $\Delta^{++}$  (blue circles). They are compared with results obtained using IQCD [41, 42] [green squares, red triangles, respectively – different results correspond to different lattice setups]; a  $\chi$ QSM [50] – black stars; chiral perturbation theory ( $\chi$ PT) [43] – purple down triangle; a relativistic constituent quark model (RCQM) [44] – brown diamond; light cone sum rules (LCSR) [46] – cyan cross; and a perturbative chiral quark model (PTQM) [49] – gold asterisk.

**Table 1** Referring to Fig. 2, separated diagram contributions (in %) to  $g_1(0)$ ,  $g_3(0)$ ,  $h_1(0)$ ,  $h_3(0)$  and  $G_{\pi\Delta\Delta}(0)$ ,  $H_{\pi\Delta\Delta}(0)$ . Diagram (1):  $\langle J \rangle_q^A$  – weak-boson strikes dressed-quark with axialvector diquark spectator. Diagram (2):  $\langle J \rangle_{qq}^{AA}$  – weak-boson strikes axialvector diquark with dressed-quark spectator. Diagram (4):  $\langle J \rangle_{ex}$  – weak-boson strikes dressed-quark “in-flight” between one diquark correlation and another. Diagrams (5) and (6):  $\langle J \rangle_{sg}$  – weak-boson couples inside the diquark correlation amplitude. The listed uncertainties reflect the impact of  $\pm 5\%$  variations in the diquark masses in Eq. (14), e.g.,  $0.57_{10\mp} \Rightarrow 0.57 \mp 0.10$ .

	$\langle J \rangle_q^A$	$\langle J \rangle_{qq}^{AA}$	$\langle J \rangle_{ex}$	$\langle J \rangle_{sg}$
$g_1(0)$	$0.57_{10\mp}$	$0.16_{1\pm}$	$0.27_{9\pm}$	0
$g_3(0)$	$0.56_{11\mp}$	$0.16_{1\pm}$	$0.39_{7\pm}$	$-0.10_{1\pm}$
$h_1(0)$	$0.52_{7\mp}$	$0.26_{1\pm}$	$0.22_{5\pm}$	0
$h_3(0)$	$0.55_{7\mp}$	$0.26_{1\pm}$	$0.21_{5\pm}$	$-0.019_{3\pm}$
$G_{\pi\Delta\Delta}(0)$	$0.55_{11\mp}$	$0.16_{1\pm}$	$0.40_{8\pm}$	$-0.10_{2\pm}$
$H_{\pi\Delta\Delta}(0)$	$0.54_{7\mp}$	$0.24_{1\pm}$	$0.24_{6\pm}$	$-0.020_{3\pm}$

large IQCD uncertainties, one can only conclude that the lattice results are qualitatively consistent with our prediction. On the other hand, in this case, one sees that the  $\chi$ QSM result is uniformly lower than our prediction.

Recalling now that  $g_3$  is kindred to the nucleon induced pseudoscalar form factor,  $G_P(x)$ , one may expect a version of the pion pole dominance (PPD) approximation to be valid. We find this to be true. Indeed, as demonstrated by the comparison drawn in Fig 3B, to a



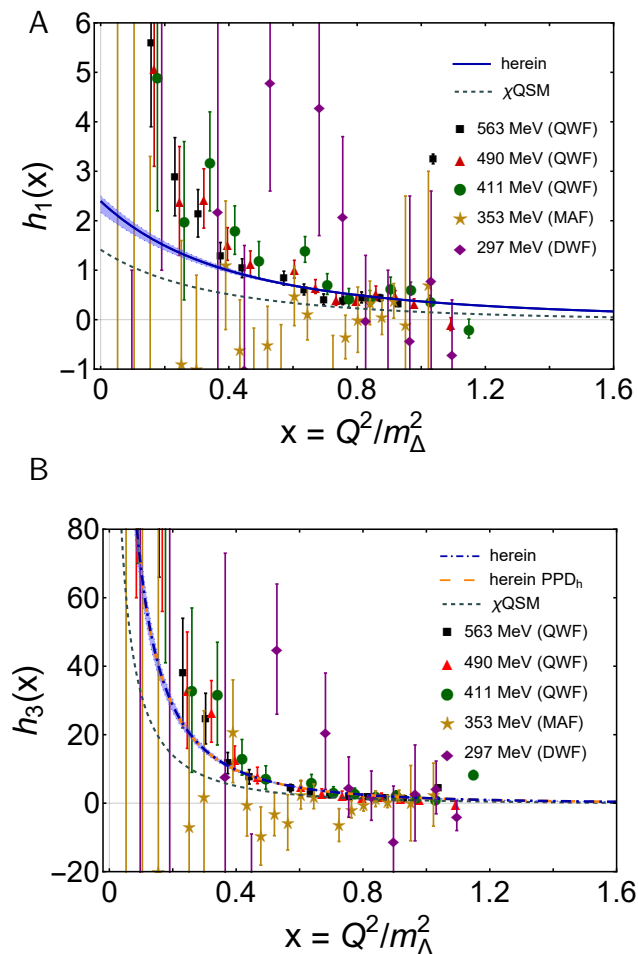


**Fig. 5** Panel A.  $h_1(x)$  calculated herein – blue curve within lighter uncertainty band. Panel B.  $h_3(x)$  calculated herein – dot-dashed blue curve within lighter uncertainty band; and long-dashed orange curve – PPD approximation, Eq. (18), employing our CSM result for  $h_1(x)$ . Comparisons in both panels: IQCD results [41] – QWF [black squares –  $m_\pi = 563$  MeV, red triangles –  $m_\pi = 490$  MeV, green circles –  $m_\pi = 411$  MeV], MAF [golden stars –  $m_\pi = 353$  MeV], DWF [purple diamonds –  $m_\pi = 297$  MeV]; and  $\chi$ QSM result [50] – short-dashed gray curve.

good level of accuracy, one can write

$$g_3(x) \approx \frac{4}{x + m_\pi^2/m_\Delta^2} g_1(x), \quad (17)$$

reproducing the form of the nucleon result [14, 15]. One can therefore consider Eq. (17) to be useful as an internal consistency check on calculations of  $\Delta$ -baryon axial form factors. As such, it may profitably be used, *e.g.*, to analyse the results in Refs. [41, 42, 50]. We present a detailed discussion of the origin and applicability of Eq. (17) in Sec. 4.3.

In Row 2 of Table 1, referring to Fig. 2, we list the relative strengths of each diagram contribution to  $g_3(0)$ . Once again, Diagram (1), with the weak boson striking the dressed quark in association with a spectator

axialvector diquark, is the dominant contributor; Diagram (2) and (4) contributions are significant; and in this case, the seagull terms act to cancel some of the Diagram (4) strength.

Our predictions for the remaining two  $\Delta$ -baryon axial form factors are drawn in Fig. 5: accurate interpolations of the central results are obtained using Eqs. (E.53) – (E.55), with the coefficients in Table 2.

Once more, the figures compare our predictions with the only other available calculations [41, 50]. For these two form factors, the IQCD uncertainties are especially large; so, little can be concluded from the numerical comparison. Qualitatively, however, there are significant disagreements. Ref. [41] argues that  $h_1$  should exhibit a pion simple pole and  $h_3$  a pion double pole. We disagree with these statements. Reviewing the projection matrices, Eq. (B.15), and the associated coefficients, Eq. (B.17), it is immediately apparent that, like  $g_1$ , which is regular,  $h_1$  only receives contributions from  $s_{3,4}$ , *i.e.*, it is entirely determined by the  $Q$ -transverse part of the  $\Delta$ -baryon axial current; hence, cannot contain a pion pole. Turning to  $h_3$ , insofar as projection matrices are concerned, this form factor is akin to  $g_3$ ; so, must express the same pion simple pole structure.

In support of these observations we note that whilst the  $\chi$ QSM results are not in quantitative agreement with our predictions, their qualitative pion pole structure predictions are consistent:  $h_1$  is regular and  $h_3$  exhibits a simple pole. On the domain depicted, the  $\chi$ QSM results for  $h_{1,3}(x)$  are uniformly smaller than our predictions. We find  $h_1(0) = 2.35(17)$ , whereas the  $\chi$ QSM result is  $h_1(0) = 1.42$ .

Like  $g_{1,3}$ , the characters of  $h_{1,3}$  are kin to  $G_{A,P}$  for the nucleon. Therefore, once again, one should anticipate a PPD relation, *viz.*

$$h_3(x) \approx \frac{4}{x + m_\pi^2/m_\Delta^2} h_1(x). \quad (18)$$

In Fig 5B, this formula is clearly shown to provide a good approximation. A detailed discussion of the origin and applicability of Eq. (18) is presented in Sec. 4.3.

In the third and fourth rows of Table 1, we list the relative strengths of each current diagram contribution to  $h_{1,3}(0)$ . There are gross similarities with the  $g_{1,3}(0)$  pattern. The differences are a reversal in the strengths of Diagrams (2) and (4) and a much smaller (in magnitude) seagull contribution to  $h_3(0)$  as compared with that to  $g_3(0)$ .

#### 4.2 $\pi$ - $\Delta$ form factors and GT relations

Consider now the  $\Delta$ -baryon pseudoscalar current,  $J_{5,\lambda\omega}$ . We focus on  $G_{\pi\Delta\Delta}(x)$ ,  $H_{\pi\Delta\Delta}(x)$  instead of  $\tilde{g}(x)$ ,  $\tilde{h}(x)$

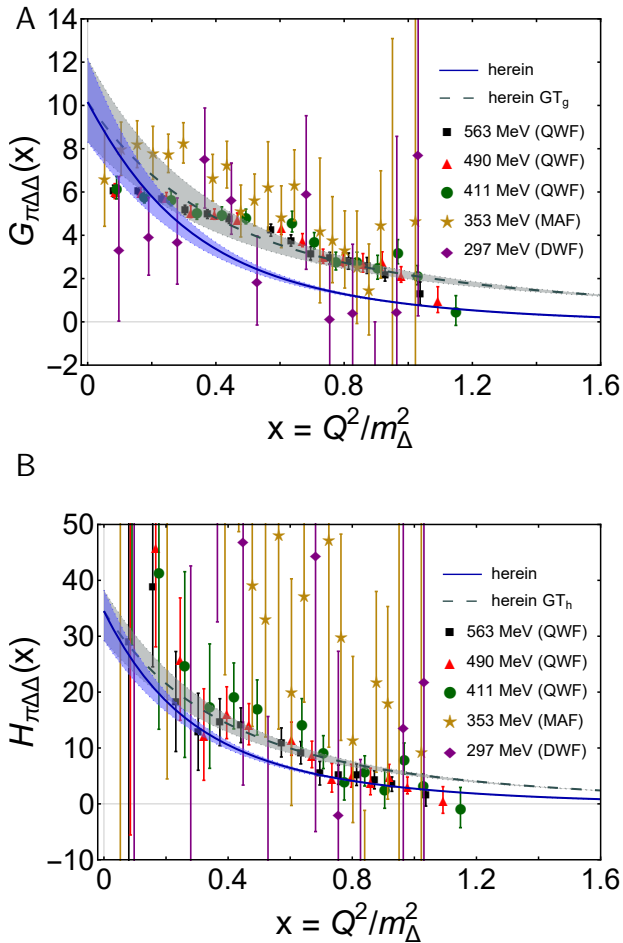


**Fig. 6** Panel A.  $G_{\pi\Delta\Delta}(x)$  calculated herein – blue curve within lighter uncertainty band; and long-dashed grey curve within lighter grey band – Eq. (23), using CSM prediction for  $g_1(x)$ . Panel B.  $H_{\pi\Delta\Delta}(x)$  calculated herein – dot-dashed blue curve within lighter uncertainty band, and long-dashed grey curve within lighter grey uncertainty band – Eq. (23), using CSM prediction for  $h_1(x)$ . Comparison, both panels: IQCD results [41] – QWF [black squares –  $m_\pi = 563$  MeV, red triangles –  $m_\pi = 490$  MeV, green circles –  $m_\pi = 411$  MeV], MAF [golden stars –  $m_\pi = 353$  MeV], and DWF [purple diamonds –  $m_\pi = 297$  MeV].

because (i) this largely eliminates sensitivity to pion mass in the results and (ii) the former functions are renormalisation point invariant, unlike the latter two.

Our CSM prediction for  $G_{\pi\Delta\Delta}(x)$  is drawn in Fig 6A: accurate interpolation of the central result is obtained using Eq. (E.53) with the coefficients in Table 2. Furthermore, on the depicted domain, a fair approximation to the result may also be obtained with a dipole function characterised by the mass scale  $\Lambda_{\pi\Delta\Delta} = 0.68(4) m_\Delta = 0.84(5) \text{ GeV}$ , *i.e.*, a soft form factor. The analogous scale for the nucleon is  $0.79 \text{ GeV}$  [15]; and just as with that analysis, our prediction for  $\Lambda_{\pi\Delta\Delta}$  is  $\sim 20\%$  larger than, hence qualitatively equivalent to, the  $\pi\Delta\Delta$  dipole mass inferred from a dynamical coupled-channels (DCC)

analysis of  $\pi N, \gamma N$  interactions [68]. This confirms that future such DCC studies may profit by implementing couplings and range parameters determined in analyses like ours.

It is worth stressing that the CSM result for  $G_{\pi\Delta\Delta}(x)$  does not exhibit a pion pole contribution and, within their larger uncertainties, the IQCD results agree with this prediction. Notwithstanding those large uncertainties, one may reasonably conclude that the CSM result is softer than that obtained using lattice regularisation.

The CSM prediction for  $H_{\pi\Delta\Delta}(x)$  is depicted in Fig 6B: accurate interpolation of the central result is obtained using Eq. (E.53) with the coefficients in Table 2. The large IQCD uncertainties make it difficult to draw conclusions from any comparison. It is plain, however, that the CSM prediction is a regular function and although Ref. [41] argues for a pion simple pole in this function, there is little signal of this in the lattice results.

Any sensible calculation of  $G_{\pi\Delta\Delta}(x)$  and  $H_{\pi\Delta\Delta}(x)$  should satisfy the GT relations, Eqs. (13). Checking this, we obtain

$$G_{\pi\Delta\Delta}(0) = 10.16(1.83) \\ \text{cf. } \frac{m_\Delta}{f_\pi} g_1(0) = 10.42(1.32), \quad (19a)$$

$$H_{\pi\Delta\Delta}(0) = 34.50(3.74) \\ \text{cf. } \frac{m_\Delta}{f_\pi} h_1(0) = 34.48(2.49); \quad (19b)$$

so, our results comply with the GT constraints.

Extrapolating  $G_{\pi\Delta\Delta}$  and  $H_{\pi\Delta\Delta}$  to  $Q^2 = -m_\pi^2$ , we find the two distinct  $\pi\Delta$  couplings

$$g_{\pi\Delta\Delta} := G_{\pi\Delta\Delta}(Q^2 = -m_\pi^2) = 10.46(1.88), \quad (20a)$$

$$h_{\pi\Delta\Delta} := H_{\pi\Delta\Delta}(Q^2 = -m_\pi^2) = 35.73(3.75). \quad (20b)$$

Regarding  $g_{\pi\Delta\Delta}$ , a forty-year-old near-threshold  $\pi^- p \rightarrow \pi^+ \pi^- n$  experiment places only a very loose constraint [69]:  $1.1 \lesssim g_{\pi\Delta\Delta} \lesssim 30$ . One may also compare with model calculations:  $g_{\pi\Delta\Delta} \approx 14.3$  [37, quark model – Eq. (B.21)];  $(9/5)g_{\pi NN} = 23.7(6)$  [38, baryon  $1/N_c$ ];  $11.8(2.0)$  [39, LCSR];  $12.0$  [45, current parametrisation];  $12.0$  [47, AdS/QCD model];  $15.88(6.04)(5.12)$  [48,  $\chi$ PT]. An error-weighted average of these results is  $g_{\pi\Delta\Delta}^{\text{ewa}} = 12.5(1.6)$ , with which our prediction is well aligned. (For results with no or an unrealistic error, we introduced an uncertainty equal to the relative error in the mean of the central values = 40%.) Including our prediction in the analysis, the result is

$$g_{\pi\Delta\Delta}^{\text{ewa}} = 11.6(1.2). \quad (21)$$

For comparison,  $g_{\pi NN} = 13.2(3)$  [15, Fig. 11a].

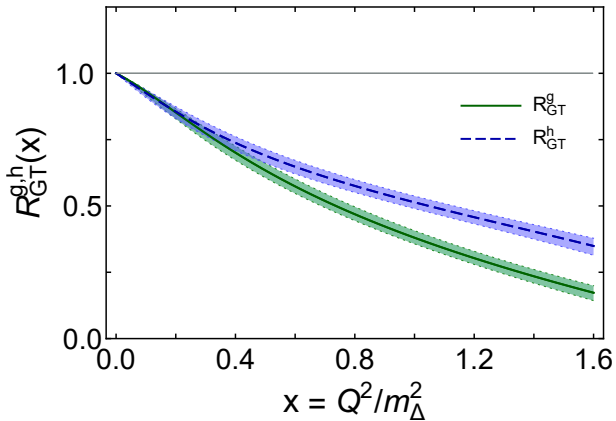


**Fig. 7** GT ratios in Eq. (24):  $R_{\text{GT}}^g(x)$  – solid green curve within lighter uncertainty band; and  $R_{\text{GT}}^h(x)$  – dashed blue curve within lighter uncertainty band.

Using Eqs. (19), (20), one can calculate two corresponding Goldberger-Treiman discrepancies:

$$\Delta_{\text{GT}}^g := 1 - \frac{G_{\pi\Delta\Delta}(0)}{G_{\pi\Delta\Delta}(-m_\pi^2)} = 0.029(0), \quad (22a)$$

$$\Delta_{\text{GT}}^h := 1 - \frac{H_{\pi\Delta\Delta}(0)}{H_{\pi\Delta\Delta}(-m_\pi^2)} = 0.035(3). \quad (22b)$$

These differences measure the deviation of the on-shell results for  $G_{\pi\Delta\Delta}$ ,  $H_{\pi\Delta\Delta}$  from their chiral limit values. Evidently, these discrepancies are modest and commensurate with that predicted for the nucleon [15]: 0.030(1).

We would like to stress that symmetry only requires that the GT relations, Eqs. (13), are satisfied on  $x \simeq 0$ . To illustrate their domain of approximate utility, the panels in Fig. 6 also display the following two functions:

$$G'_{\pi\Delta\Delta}(x) = \frac{m_\Delta}{f_\pi} g_1(x), \quad H'_{\pi\Delta\Delta}(x) = \frac{m_\Delta}{f_\pi} h_1(x). \quad (23)$$

Where these curves overlap with our predictions for  $G_{\pi\Delta\Delta}(x)$ ,  $H_{\pi\Delta\Delta}(x)$ , one has a domain of useful approximation. That domain is small. A somewhat different conclusion is suggested by Ref. [41, Figs. 9, 10], with the GT relations being satisfied (within large uncertainties) on a material  $x$  domain. However, those outcomes are likely the result of lattice artefacts.

In order to explicate the domain of approximate validity, Fig. 7 depicts the following GT ratios:

$$R_{\text{GT}}^g(x) = \frac{f_\pi G_{\pi\Delta\Delta}(x)}{m_\Delta g_1(x)}, \quad R_{\text{GT}}^h(x) = \frac{f_\pi H_{\pi\Delta\Delta}(x)}{m_\Delta h_1(x)}. \quad (24)$$

These curves decreasing monotonically from unity as  $x$  increases from zero, each deviating from unity by more than 10% on  $x > 0.14$  and more than 20% on  $x > 0.29$ .

In the last two rows of Table 1, referring to Fig. 2, we list the relative strengths of each diagram contribution to  $G_{\pi\Delta\Delta}(0)$ ,  $H_{\pi\Delta\Delta}(0)$ , respectively. Notably, the breakdown for  $G_{\pi\Delta\Delta}(0)$  is very much like that for  $g_3(0)$ ; and the separation for  $H_{\pi\Delta\Delta}(0)$  strongly resembles the  $h_3(0)$  pattern. Similar statements were also true for the nucleon induced-pseudoscalar and true pseudoscalar form factors,  $G_{P,5}$ , respectively – see Ref. [15, Table 1]; and the explanation is the same. Namely, if one focuses on the singular (longitudinal) part of the axial current,  $J_{5\mu,\lambda\omega}$ , which provides the overwhelmingly dominant contribution to  $g_3(0)$ ,  $h_3(0)$ , and compares the related projection matrices for  $g_3$ ,  $h_3$ ,  $\tilde{g}$ ,  $\tilde{h}$  – see Eqs. (B.16), (B.17), (B.19), (B.20), then the following correspondences become apparent:

$$g_3(0) \approx \tilde{g}(0) \propto G_{\pi\Delta\Delta}(0), \quad (25a)$$

$$h_3(0) \approx \tilde{h}(0) \propto H_{\pi\Delta\Delta}(0). \quad (25b)$$

Hence, the relative strengths of different diagram contributions must be approximately the same in each case.

#### 4.3 Dissecting the PCAC and PPD relations

Equation (7) is an operator relation. Thus, any physical results for axialvector and pseudoscalar form factors should satisfy Eqs. (10). In Ref. [15], a theoretical framework was constructed which guarantees the analogous outcomes for the nucleon – see Appendix D therein for a proof. Herein, we have adapted that approach to the  $\Delta$ -baryon; and, using the explicit expressions for the current in Fig. 2, written in Appendix D, and following the same steps as for the nucleon, one may readily establish algebraically that all our results comply with Eqs. (10).

Notwithstanding that, numerical verification is also useful, not least because it reveals the level of accuracy in our calculations. Therefore, consider the following two  $\Delta$ -baryon PCAC ratios:

$$R_{\text{PCAC}}^g = \frac{4g_1}{x g_3 + 4\tilde{g} m_q/m_\Delta}, \quad (26a)$$

$$R_{\text{PCAC}}^h = \frac{4h_1}{x h_3 + 4\tilde{h} m_q/m_\Delta}. \quad (26b)$$

Our calculated results for both are drawn in Fig. 8: on the entire displayed domain, both curves are practically indistinguishable from unity. We reiterate that these outcomes are parameter independent.

Two PPD relations were introduced and discussed in Sec. 4.1 – Eqs. (17), (18). In order to draw additional links with nucleon properties, we reconsider them here



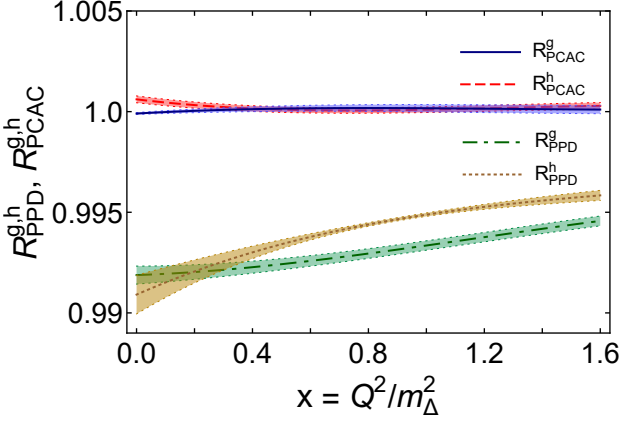


**Fig. 8** Numerical verification of the PCAC relations in Eqs. (26): solid blue curve within lighter band – Eq. (26a); and dashed red curve within lighter band – Eq. (26b). In addition, numerical check of the PPD relations in Eqs. (27): dot-dashed green curve within lighter band – Eq. (27a); and dotted gold curve within lighter band – Eq. (27b). As usual, the bands indicate the response to a  $\pm 5\%$  variation in the mass of the axialvector diquark.

from a different perspective. Consider the following two ratios ( $\mu_\Delta^\pi = m_\pi^2/m_\Delta^2$ ):

$$R_{\text{PPD}}^g = \frac{4g_1}{(x + \mu_\Delta^\pi) g_3}, \quad (27a)$$

$$R_{\text{PPD}}^h = \frac{4h_1}{(x + \mu_\Delta^\pi) h_3}. \quad (27b)$$

The calculated curves are depicted in Fig. 8. Similar to the nucleon result [15, Fig. 8], these curves lie  $\lesssim 1\%$  below unity on  $x \simeq 0$  and grow toward unity as  $x$  increases. The behaviour is genuine, can readily be explained within our quark+diqurk framework, and is actually universal for all baryon PPD ratios. We will exemplify these things using  $R_{\text{PPD}}^g$ .

First note that in the chiral limit,  $R_{\text{PPD}}^g$  – Eq. (27a) and  $R_{\text{PCAC}}^g$  – Eq. (26a) are equivalent; hence, both are precisely unity:

$$R_{\text{PPD}}^{g,m_q=0} = R_{\text{PCAC}}^{g,m_q=0} = \frac{4g_1^{m_q=0}}{xg_3^{m_q=0}} = 1. \quad (28)$$

Second, considering the dressed-quark vertex – Eq. (D.39a), the diquark vertex – Eq. (D.43), and the seagull terms – Eqs. (D.50a), (D.50c), one can establish that the axialvector current,  $J_{5\mu,\lambda\omega}$ , is a sum of well-defined regular and singular pieces, in consequence of which one may write

$$g_1 = g_{1,\text{regular}} + g_{1,\text{singular}}, \quad (29a)$$

$$g_3 = g_{3,\text{regular}} + g_{3,\text{singular}}. \quad (29b)$$

Furthermore, the regular part of  $J_{5\mu,\lambda\omega}$  does not depend explicitly on the current-quark mass,  $m_q$ , and the

singular part is proportional to  $Q_\mu/(Q^2 + m_\pi^2)$ ; hence, is purely longitudinal and does not contribute to  $g_1$  – see Eqs. (B.15) – (B.17). Consequently,

$$g_1 = g_{1,\text{regular}} = g_{1,\text{regular}}^{m_q=0} = g_1^{m_q=0}. \quad (30)$$

Extending these considerations,

$$g_{3,\text{regular}} = g_{3,\text{regular}}^{m_q=0}, \quad (31a)$$

$$(Q^2 + m_\pi^2)g_{3,\text{singular}} = Q^2 g_{3,\text{singular}}^{m_q=0} =: m_\Delta^2 \mathcal{G}, \quad (31b)$$

where  $\mathcal{G}$  is a regular function. Inserting Eqs. (30), (31) into Eq. (27a) and using Eq. (28), we arrive at

$$R_{\text{PPD}}^g = \frac{4g_1^{m_q=0}}{xg_3^{m_q=0} + g_{3,\text{regular}}^{m_q=0}\mu_\Delta^\pi} \quad (32a)$$

$$= \frac{xg_3^{m_q=0}}{xg_3^{m_q=0} + g_{3,\text{regular}}^{m_q=0}\mu_\Delta^\pi} \quad (32b)$$

$$= \frac{xg_{3,\text{regular}}^{m_q=0} + \mathcal{G}}{xg_{3,\text{regular}}^{m_q=0} + \mathcal{G} + g_{3,\text{regular}}^{m_q=0}\mu_\Delta^\pi}. \quad (32c)$$

Plainly, on  $x \simeq 0$ ,  $R_{\text{PPD}}^g$  must differ from unity because of the denominator term  $\propto \mu_\Delta^\pi = m_\pi^2/m_\Delta^2$ ; and the size of the correction diminishes as  $\mu_\Delta^\pi/x$  with increasing  $x$ .

The size of the  $x \simeq 0$  deviation is readily estimated algebraically. Using Eqs. (10a), (11a), (13a), one finds

$$g_3(x) = \frac{4}{x}g_1(x) \left[ 1 - \frac{\mu_\Delta^\pi}{x + \mu_\Delta^\pi} \frac{G_{\pi\Delta\Delta}(x)/G_{\pi\Delta\Delta}(0)}{g_1(x)/g_1(0)} \right]. \quad (33)$$

Now, referring to Eq. (27a), define

$$g_3^\pi(x) = \frac{4}{x + \mu_\Delta^\pi} g_1(x) = \frac{4}{x} g_1(x) \left[ 1 - \frac{\mu_\Delta^\pi}{x + \mu_\Delta^\pi} \right]. \quad (34)$$

Then,

$$R_{\text{PPD}}^g \equiv \frac{g_3^\pi(x)}{g_3(x)} \quad (35a)$$

$$= \left[ 1 + \frac{\mu_\Delta^\pi}{x} \left( 1 - \frac{G_{\pi\Delta\Delta}(x)/G_{\pi\Delta\Delta}(0)}{g_1(x)/g_1(0)} \right) \right]^{-1}. \quad (35b)$$

Consequently,

$$R_{\text{PPD}}^g(x \simeq 0) = \left( 1 + \frac{1}{6} m_\pi^2 [r_{G_{\pi\Delta\Delta}}^2 - r_{g_1}^2] \right)^{-1}, \quad (36)$$

where  $r_{G_{\pi\Delta\Delta}}$ ,  $r_{g_1}$  are form factor radii, defined, via ( $F \in \{G_{\pi\Delta\Delta}, g_1\}$ )

$$r_F^2 = -6 \frac{1}{m_\Delta^2} \frac{d}{dx} \frac{G_F(x)}{G_F(0)} \Big|_{x=0}. \quad (37)$$

Using our interpolations of  $G_{\pi\Delta\Delta}$ ,  $g_1$  – Appendix E, one obtains  $r_{G_{\pi\Delta\Delta}} = 0.60(1)$  fm,  $r_{g_1} = 0.53(1)$  fm; and inserting these values into Eq. (36):

$$R_{\text{PPD}}^g(Q^2 \simeq 0) = 0.993(0). \quad (38)$$

This result matches and explains that in Fig. 8. (It is worth noting here that  $r_{g_1} = 0.78(1) r_A^N$ , *i.e.*, the axial radius of the  $\Delta$ -baryon is roughly 20% smaller than that of the nucleon.)

The behaviour of the second PPD ratio,  $R_{\text{PPD}}^h$  – Eq. (27b), can similarly be explained. Using Eq. (37),  $r_{H_{\pi\Delta\Delta}} = 0.64(2) \text{ fm}$ ,  $r_{h_1} = 0.56(3) \text{ fm}^{-1}$ ; hence,

$$R_{\text{PPD}}^h(x \simeq 0) = \left(1 + \frac{1}{6} m_\pi^2 [r_{H_{\pi\Delta\Delta}}^2 - r_{h_1}^2]\right)^{-1} \quad (39a)$$

$$= 0.992(1). \quad (39b)$$

As expected, this value matches and explains the associated result in Fig. 8.

## 5 Axial charge flavour separation

As noted in the Introduction, the Poincaré-covariant Faddeev wave functions of  $\Delta$ -baryons are simpler than that of the proton because  $\Delta$  states only contain isovector-axialvector diquarks whereas the proton also contains isoscalar-scalar diquarks that can mix with isovector-axialvector diquarks under weak interactions. Nevertheless, Poincaré-covariant  $\Delta$ -baryon wave functions are not trivial: in addition to S-wave components, they contain significant P-wave and  $\text{S} \otimes \text{P}$ -interference components [21, Fig. 8a]. Consequently, as with the proton [70], there is no reference frame in which the total  $J = \frac{3}{2}$  of the  $\Delta$ -baryon is merely the sum of three parallel  $J = \frac{1}{2}$  quark spins.

These remarks can be quantified by presenting a flavour decomposition of  $g_1^\Delta(0)$ . Consider first the  $\Delta^{++}$ . In this case, only the  $u$ -quark contributes. There are three  $u$  quarks; so, one can write

$$g_A^{\Delta^{++}} =: 3g_A^{\Delta^u} = 3 \times 0.71(9) \Rightarrow g_A^{\Delta^u} = 0.71(9), \quad (40)$$

where the last few steps express results of our calculations – see Eq. (16). (Here, we have explicitly removed the valence quark number,  $n_u^{\Delta^{++}} = 3$ , from the charge.) Our prediction may be compared with a IQCD estimate of this charge [42]:  $g_A^{\Delta^u} = 0.59(16)$ . They agree within mutual uncertainties. (Recall Fig. 4, in which IQCD results are systematically lower than other estimates.) The isoscalar axial charge of any hadron is invariant under leading-order QCD evolution [70, 71].

In any simple  $\text{SU}(4)$  quark model, the result here would be  $3 \times g_A^{\text{QM}}$ ,  $g_A^{\text{QM}} = 1$ . Two conclusions are immediately apparent: (*i*) owing to spin–flavour–relative-momentum correlations expressed in the Faddeev wave function, which break  $\text{SU}(4)$  symmetry, the axial charge of each dressed quark within the  $\Delta$ -baryon is “quenched”; and (*ii*), consequently, dressed-quarks in the  $\Delta^{++}$  carry

only  $\approx 71\%$  of the baryon’s total spin. In the proton, the result is  $\approx 65\%$ .

Turning to the  $\Delta^-$ , only  $d$  quarks contribute. In this case, using Eqs. (A.13), we find (in the isospin symmetry limit)

$$g_A^{\Delta^-} = -g_A^{\Delta^{++}} =: -3g_A^{\Delta^d} \Rightarrow g_A^{\Delta^d} = 0.71(9). \quad (41)$$

Evidently,

$$\frac{g_A^{\Delta^d}}{g_A^{\Delta^u}} = 1 \text{ cf. } \frac{g_A^{p_d}}{g_A^{p_u}} = -0.64(4), \quad (42)$$

where the last equality expresses the result for the analogous ratio in the proton [16]. (Recall, herein we have removed the in-hadron valence quark number from the charge:  $n_u^p = 2$ ,  $n_d^p = 1$ .) The change in sign and relative magnitudes revealed by Eq. (42) highlight the impacts of the additional correlations within the proton wave function on the effective axial charges of its dressed quarks.

## 6 Summary and perspective

Using a Poincaré-covariant quark+diquark Faddeev equation treatment of  $\Delta$ -baryons and weak interaction currents that guarantee consistency with relevant Ward-Green-Takahashi identities, we delivered the first continuum predictions for all six  $\Delta$ -baryon elastic weak form factors. In doing so, we unified them with the three analogous nucleon form factors, treated using the same framework elsewhere [15]. Concerning  $\Delta$ -baryons, there are two distinct classes of partial conservation of axial current (PCAC) and related Goldberger-Treiman (GT) relations, involving form factor sets  $(g_1, g_3, G_{\pi\Delta\Delta})$ ,  $(h_1, h_3, H_{\pi\Delta\Delta})$ , and we provided a detailed discussion of their realisations within our framework.

The  $\Delta$ -baryon  $g_1$  axial form factor is analogous to the nucleon  $G_A$  form factor. Our calculations show that it can reliably be approximated by a dipole function on  $0 < Q^2 \lesssim 1.6m_\Delta^2$ , where  $m_\Delta$  is the  $\Delta$ -baryon mass, normalised by an axial charge, which takes the value  $g_A^{\Delta^+} = 0.71(9)$  [Eqs. (15), (16)]. The dipole mass,  $m_A^\Delta = 0.95(2)m_\Delta$ , is a little larger than that found in analysing  $G_A$ . Our prediction for  $g_1(Q^2)$  is consistent with available results from lattice-regularised QCD (IQCD) [40, 41] [Fig. 3A]. It is also more precise and, therefore, given the accuracy of the kindred prediction for  $G_A(Q^2)$ , quite likely more reliable.

Regarding the  $g_3$  form factor, which is an analogue of the nucleon induced-pseudoscalar form factor,  $G_P$ , we showed that it possesses a first-order pion pole. Further in this connection, to a good level of accuracy,  $g_3$

and  $g_1$  are related by a pion pole dominance (PPD) approximation [Eq. (17), Fig. 8]; again, just as one finds for the kindred nucleon form factors.

Turning to the other class of form factors, we predicted that  $h_1$  is a regular function and, like  $g_3$  and  $G_P$ ,  $h_3$  exhibits a first-order pion pole [Fig. 5]. In these statements, which are supported by algebraic analyses, we differ with those inferred from lQCD [40, 41]. Notably, the only other calculation of these form factors supports our findings [50]. Unsurprisingly, given the symmetry preserving character of our analysis, to a good level of accuracy, a PPD approximation links  $h_1$  and  $h_3$  [Eq. (18), Fig. 8].

The  $\Delta$ -baryon pseudoscalar currents are best characterised in terms of renormalisation point invariant  $\pi\Delta\Delta$  form factors:  $G_{\pi\Delta\Delta}$ ,  $H_{\pi\Delta\Delta}$  [Sec. 4.2]. We find, algebraically and numerically, that both are regular functions, just as is  $G_{\pi NN}$ . These results challenge the lQCD claim that  $H_{\pi\Delta\Delta}$  has a pion simple pole [41]. Regarding  $G_{\pi\Delta\Delta}$ , there are many estimates of the  $Q^2 + m_\pi^2 = 0$  (pion on-shell) value. We predict  $g_{\pi\Delta\Delta} = 10.46(1.88)$ , which compares favourably with an error weighted average of model estimates, *viz.* 12.5(1.6). The on-shell value of the second  $\pi\Delta\Delta$  form factor is  $h_{\pi\Delta\Delta} = 35.73(3.75)$ . Our results are consistent with the GT symmetry constraints – algebraically and numerically [Eqs. (19)]: of course, these constraints only apply on  $Q^2/m_\Delta^2 \simeq 0$ .

Partly as a check on our numerical methods, we verified that the PCAC relations – expressing key symmetries of Nature and proved algebraically within our framework, are also satisfied numerically in our calculations: the mismatch is never more than 0.1% [Fig. 8]. We also showed that the two  $\Delta$ -baryon PPD approximations are satisfied at better than 1% on  $Q^2 > 0$ , explaining that the  $Q^2/m_\Delta^2 \simeq 0$  discrepancy is real and natural [Sec. 4.3].

Having established the hardness of our framework, we completed a flavour decomposition of the  $\Delta$ -baryon axial charges [Sec. 5]. Owing to the simplicity of  $\Delta$ -baryon Poincaré-covariant wave functions when compared to that of the proton, this was relatively straightforward. The analysis predicts that, at the hadron scale, the dressed-quarks carry 71% of the  $\Delta$ -baryon spin, with the remainder stored in quark+diquark orbital angular momentum. In the proton, the analogous fraction is  $\approx 65\%$ . Notably, too, the additional correlations within the proton wave function produce different quenchedings of the  $u$  and  $d$  quark axial charges.

As stated at the outset, now, with reliable predictive tool established, the natural next step is to calculate the form factors that characterise weak-interaction induced  $N \rightarrow \Delta(1232)$  transitions. Reliable predictions for these transition form factors are important in order to under-

stand modern neutrino-nucleus scattering experiments that seek physics beyond the Standard Model. Consequently, many estimates exist. However, none may claim to deliver a fully Poincaré-covariant treatment of the process, which, simultaneously, unifies it with a large array of electroweak properties of the nucleon and  $\Delta$ -baryons themselves.

A longer term goal is elimination of the quark+diquark approximation to the Faddeev kernel, replacing the resulting Faddeev amplitude with the solution of a truly three-body equation. Following Refs. [72, 73], this is achievable. However, it must also be realistic; and that challenge may require an approach which goes beyond the leading-order continuum Schwinger function method truncation of the baryon three-body problem.

*Acknowledgments.* We are grateful to Y.-S. Jun and H.-C. Kim for providing us with the  $\chi$ QSM results in Ref. [50] and for constructive comments from Z.-F. Cui, V. I. Mokeev and D.-L. Yao. Work supported by: National Natural Science Foundation of China (grant nos. 12135007 and 12247103); Nanjing University of Posts and Telecommunications Science Foundation (grant no. NY221100); and Deutsche Forschungsgemeinschaft (DFG) (grant no. FI 970/11-1).

## Appendix A: Colour and flavour coefficients

The explicit form of the  $\Delta$ -baryon Faddeev equation pictured in Fig. 1 is

$$\begin{aligned} \Psi_{\mu\nu}^\Delta(p; P) \\ = \int_{dk} \mathcal{X}_{\mu\lambda}^\Delta(p, k, P) S(\tilde{k}_q) \mathcal{D}_{\lambda\sigma}^{1+}(\tilde{k}_d) \Psi_{\sigma\nu}^\Delta(k; P), \end{aligned} \quad (\text{A.1})$$

where  $\int_{dk} := \int d^k p / (2\pi)^4$ ; and the Faddeev equation quark-exchange kernel is

$$\mathcal{X}_{\mu\lambda}^\Delta(p, k, P) = \Gamma_\lambda^{1+}(k_r) S^T(q) \bar{\Gamma}_\mu^{1+}(p_r), \quad (\text{A.2})$$

with momenta ( $\eta = 1/3$ ,  $\hat{\eta} = 1 - \eta$ )

$$\begin{aligned} \tilde{p}_q &= p + \eta P, & \tilde{k}_q &= k + \eta P, \\ \tilde{p}_d &= -p + \hat{\eta} P, & \tilde{k}_d &= -k + \hat{\eta} P, \\ q &= \tilde{p}_d - \tilde{k}_q, \\ p_r &= \frac{\tilde{k}_q - q}{2}, & k_r &= \frac{\tilde{p}_q - q}{2}. \end{aligned} \quad (\text{A.3})$$

Taking the product of the flavour and colour matrices in Eq. (A.1), which are given in Eqs. (C.26), (C.32), and subsequently projecting onto the isospinors of the

specified  $\Delta$  state:

$$e_{\Delta^{++}} = \begin{pmatrix} 1 \\ 0 \\ 0 \\ 0 \end{pmatrix}, \quad e_{\Delta^+} = \begin{pmatrix} 0 \\ 1 \\ 0 \\ 0 \end{pmatrix}, \quad (\text{A.4a})$$

$$e_{\Delta^0} = \begin{pmatrix} 0 \\ 0 \\ 1 \\ 0 \end{pmatrix}, \quad e_{\Delta^-} = \begin{pmatrix} 0 \\ 0 \\ 0 \\ 1 \end{pmatrix}, \quad (\text{A.4b})$$

one finds that the colour-flavour coefficient of  $\Delta$ -baryon Faddeev equation, Eq. (A.1), is “−1”.

For the form factor diagrams of Fig. 2, each of the flavour coefficients must be calculated separately. One has

$$\sum_{k,l=1}^3 \left[ \delta^{kl} (s_f^k)^\dagger \left( \frac{\tau^j}{2} \right) (s_f^l) \right], \quad (\text{A.5})$$

for the probe-quark diagram – Diagram (1), where  $\{s_f^k | k = 1, 2, 3\}$  are given in Eq. (C.34);

$$\sum_{k,l=1}^3 \left[ (s_f^k)^\dagger (s_f^l) \text{tr} \left[ (t_f^k)^\dagger \left( \frac{\tau^j}{2} \right)^\dagger \right] \right], \quad (\text{A.6})$$

for the probe-diquark diagram – Diagram (2), where the diquark flavour matrices are given in Eq. (C.27); and

$$\sum_{k,l=1}^3 \left[ (s_f^k)^\dagger (t_f^l) \left( \frac{\tau^j}{2} \right)^\dagger (t_f^k)^\dagger (s_f^l) \right], \quad (\text{A.7})$$

for the exchange diagram – Diagram (4).

The seagull case is somewhat more complicated because one needs to treat the bystander and exchange quark legs separately. Considering Diagram (5), the exchange leg is

$$\sum_{k,l=1}^3 \left[ (s_f^k)^\dagger (t_f^l) \left( \frac{\tau^j}{2} \right)^\dagger (t_f^k)^\dagger (s_f^l) \right] \quad (\text{A.8})$$

and the bystander leg is

$$\sum_{k,l=1}^3 \left[ (s_f^k)^\dagger \left( \frac{\tau^j}{2} \right) (t_f^l) (t_f^k)^\dagger (s_f^l) \right]. \quad (\text{A.9})$$

For the conjugation, Diagram (6), the exchange leg is

$$\sum_{k,l=1}^3 \left[ (s_f^k)^\dagger (t_f^l) \left( \frac{\tau^j}{2} \right)^\dagger (t_f^k)^\dagger (s_f^l) \right] \quad (\text{A.10})$$

and the bystander,

$$\sum_{k,l=1}^3 \left[ (s_f^k)^\dagger (t_f^l) (t_f^k)^\dagger \left( \frac{\tau^j}{2} \right) (s_f^l) \right]. \quad (\text{A.11})$$

Finally, again, one must project these matrices, Eqs. (A.5) – (A.11), into the required  $\Delta$ -baryon charge state using the isospin vectors in Eqs. (A.4).

The colour factors are “1” for impulse-approximation contributions – Diagrams (1) and (2), and “−1” for the exchange and seagull diagrams – Diagrams (4), (5), (6).

Using the  $\Delta^+$ -baryon as the exemplar, writing the flavour and colour factors explicitly, one has

$$J_{5(\mu),\lambda\omega}^{\Delta^+} = \frac{1}{3} \left( J_{5(\mu),\lambda\omega}^{\text{q}(1)} + J_{5(\mu),\lambda\omega}^{\text{dq}(2)} - J_{5(\mu),\lambda\omega}^{\text{ex}(4)} - J_{5(\mu),\lambda\omega}^{\text{sg}(5)} - J_{5(\mu),\lambda\omega}^{\text{sg}(6)} \right). \quad (\text{A.12})$$

Here, for additional clarity, we have included the diagram label from Fig. 2 as an additional superscript. In the isospin symmetry limit, expressions for the other  $\Delta$  states can be obtained straightforwardly:

$$J_{5(\mu),\lambda\omega}^{\Delta^{++}} = 3J_{5(\mu),\lambda\omega}^{\Delta^+}, \quad (\text{A.13a})$$

$$J_{5(\mu),\lambda\omega}^{\Delta^0} = -J_{5(\mu),\lambda\omega}^{\Delta^+}, \quad (\text{A.13b})$$

$$J_{5(\mu),\lambda\omega}^{\Delta^-} = -3J_{5(\mu),\lambda\omega}^{\Delta^+}. \quad (\text{A.13c})$$

Thus,

$$F^{\Delta^{++}} = 3F^{\Delta^+}, \quad (\text{A.14a})$$

$$F^{\Delta^0} = -F^{\Delta^+}, \quad (\text{A.14b})$$

$$F^{\Delta^-} = -3F^{\Delta^+}, \quad (\text{A.14c})$$

where  $F \in \{g_1, g_3, h_1, h_3, \tilde{g}, \tilde{h}, G_{\pi\Delta\Delta}, H_{\pi\Delta\Delta}\}$ .

## Appendix B: Extraction of the form factors

Beginning with the expressions for the  $\Delta$  axial current, Eqs. (2), (5), one can extract the four axialvector form factors by using the following projection matrices:

$$s_1 := i \text{tr}_D [J_{5\mu,\lambda\omega} \gamma_5] \hat{Q}_\mu \hat{Q}_\lambda \hat{Q}_\omega, \quad (\text{B.15a})$$

$$s_2 := i \text{tr}_D [J_{5\mu,\lambda\lambda} \gamma_5] \hat{Q}_\mu, \quad (\text{B.15b})$$

$$s_3 := \text{tr}_D [J_{5\mu,\lambda\omega} \gamma_\mu^T \gamma_5] \hat{Q}_\lambda \hat{Q}_\omega, \quad (\text{B.15c})$$

$$s_4 := \text{tr}_D [J_{5\mu,\lambda\lambda} \gamma_\mu^T \gamma_5], \quad (\text{B.15d})$$

where the trace is over Dirac indices;  $\hat{Q}_\mu = Q_\mu / \sqrt{Q^2}$ ,  $\gamma_\mu^T = \gamma_\mu - \gamma \cdot \hat{Q} \hat{Q}_\mu$ . In this case, one has

$$g_1 = \sum_{i=1}^4 c_{1i} s_i, \quad g_3 = \sum_{i=1}^4 c_{2i} s_i, \quad (\text{B.16a})$$

$$h_1 = \sum_{i=1}^4 c_{3i} s_i, \quad h_3 = \sum_{i=1}^4 c_{4i} s_i, \quad (\text{B.16b})$$

with ( $t = Q^2/[4m_\Delta^2]$ )

$$\begin{aligned}
c_{11} &= 0 = c_{12}, \\
c_{13} &= \frac{3(1+2t)}{8(1+t)^2}, & c_{14} &= \frac{-3}{8(1+t)}, \\
c_{21} &= \frac{1+4t}{4t^{3/2}(1+t)}, & c_{22} &= \frac{-1}{2t^{3/2}}, \\
c_{23} &= \frac{3(1+2t)}{8t(1+t)^2}, & c_{24} &= \frac{-3}{8t(1+t)}, \\
c_{31} &= 0 = c_{32}, \\
c_{33} &= \frac{3(5+8t[1+t])}{16t(1+t)^3}, & c_{34} &= \frac{-3(1+2t)}{8t(1+t)^2}, \\
c_{41} &= \frac{5+4t(1+2t)}{4t^{5/2}(1+t)^2}, & c_{42} &= \frac{-(1+4t)}{4t^{5/2}(1+t)}, \\
c_{43} &= \frac{3(5+8t[1+t])}{16t^2(1+t)^3}, & c_{44} &= \frac{-3(1+2t)}{8t^2(1+t)^2}.
\end{aligned} \tag{B.17}$$

Turning to the  $\Delta$ -baryon pseudoscalar current, Eqs. (4), (5), one can extract the other two form factors of interest. Using the following projection matrices:

$$\tilde{s}_1 := i\text{tr}_D[J_{5,\lambda\omega}\gamma_5]\hat{Q}_\lambda\hat{Q}_\omega, \tag{B.18a}$$

$$\tilde{s}_2 := i\text{tr}_D[J_{5,\lambda\lambda}\gamma_5], \tag{B.18b}$$

one has

$$\tilde{g} = \sum_{i=1}^2 \tilde{c}_{1i}\tilde{s}_i, \quad \tilde{h} = \sum_{i=1}^2 \tilde{c}_{2i}\tilde{s}_i, \tag{B.19}$$

with

$$\begin{aligned}
\tilde{c}_{11} &= \frac{-(1+4t)}{4t(1+t)}, & \tilde{c}_{12} &= \frac{1}{2t}, \\
\tilde{c}_{21} &= \frac{-(5+4t[1+2t])}{4t^2(1+t)^2}, & \tilde{c}_{22} &= \frac{1+4t}{4t^2(1+t)}.
\end{aligned} \tag{B.20}$$

## Appendix C: QCD-kindred framework

Since being introduced in Refs. [74–76], the QCD-kindred model for ground-state mesons and baryons that we use herein has been refined in a series of analyses that may be traced from Ref. [28]. Consistency between the various Schwinger functions involved is guaranteed through their mutual interplay in the description and prediction of hadron observables.

### Appendix C.1: Dressed quark propagator

The dressed-quark propagator is:

$$S(p) = -i\gamma \cdot p \sigma_V(p^2) + \sigma_S(p^2) \tag{C.21a}$$

$$= 1/[i\gamma \cdot p A(p^2) + B(p^2)]. \tag{C.21b}$$

Regarding light-quarks, the wave function renormalisation and dressed-quark mass:

$$Z(p^2) = 1/A(p^2), \quad M(p^2) = B(p^2)/A(p^2), \tag{C.22}$$

respectively, receive significant momentum-dependent corrections at infrared momenta [77–79]:  $Z(p^2)$  is suppressed and  $M(p^2)$  enhanced. These features are an expression of emergent hadron mass (EHM) [12, 53–55].

An efficacious parametrisation of  $S(p)$ , which exhibits the features described above, has been used extensively in hadron studies – see, *e.g.*, [63–67]. It is expressed via

$$\bar{\sigma}_S(x) = 2\bar{m} \mathcal{F}(2(x + \bar{m}^2)) + \mathcal{F}(b_1x) \mathcal{F}(b_3x) [b_0 + b_2\mathcal{F}(\epsilon x)], \tag{C.23a}$$

$$\bar{\sigma}_V(x) = \frac{1}{x + \bar{m}^2} [1 - \mathcal{F}(2(x + \bar{m}^2))], \tag{C.23b}$$

with  $x = p^2/\lambda^2$ ,  $\bar{m} = m/\lambda$ ,

$$\mathcal{F}(x) = \frac{1 - e^{-x}}{x}, \tag{C.24}$$

$\bar{\sigma}_S(x) = \lambda\sigma_S(p^2)$  and  $\bar{\sigma}_V(x) = \lambda^2\sigma_V(p^2)$ . The mass-scale,  $\lambda = 0.566$  GeV, and parameter values

$$\frac{\bar{m} \quad b_0 \quad b_1 \quad b_2 \quad b_3}{0.00897 \quad 0.131 \quad 2.90 \quad 0.603 \quad 0.185}, \tag{C.25}$$

associated with Eqs. (C.23) were fixed in analyses of light-meson observables [75, 80]. (In Eq. (C.23a),  $\epsilon = 10^{-4}$  serves only to decouple the large- and intermediate- $p^2$  domains.)

The dimensionless  $u = d$  current-mass in Eq. (C.25) corresponds to  $m_q = 5.08$  MeV and the propagator yields the following Euclidean constituent-quark mass, defined by solving  $p^2 = M^2(p^2)$ :  $M_q^E = 0.33$  GeV. The ratio  $M_q^E/m_q = 65$  is one expression of dynamical chiral symmetry breaking (DCSB), a corollary of emergent hadronic mass, in the parametrisation of  $S(p)$ . It highlights the infrared enhancement of the dressed-quark mass function.

The dressed-quark mass function generated by Eqs. (C.23) – (C.25) is drawn elsewhere [15, Fig. 13]. The image demonstrates that, although simple and introduced long beforehand, the parametrisation is a sound representation of contemporary numerical results.

The expressions in Eq. (C.23) ensure dressed-quark confinement via the violation of reflection positivity – see, *e.g.* Ref. [12, Sec. 5]. The same is true of the diquark propagators in Eq. (C.31).



## Appendix C.2: Diquark amplitude and propagator

Regarding  $\Delta$ -baryons, it is only necessary to involve isovector-axialvector diquarks [21]. Retaining just the dominant structure, their correlation amplitude is

$$\Gamma_\mu^{1+}(k; K) = ig_{1+}\gamma_\mu C \vec{t}_f \vec{H}_c \mathcal{F}(k^2/\omega_{1+}^2). \quad (\text{C.26})$$

Here,  $K$  is the diquark's total momentum;  $k$  is the relative momentum;  $\mathcal{F}$  is the function in Eq. (C.24);  $\omega_{1+}$  is a width parameter, which characterises the diquark's propagation within the baryon,  $\omega_{1+}^2 = m_{1+}^2/2$ , where  $m_{1+} = 0.89 \text{ GeV}$  is the diquark mass;  $\vec{H}_c = \{i\lambda_c^7, -i\lambda_c^5, i\lambda_c^2\}$ , with  $\{\lambda_c^k, k = 1, \dots, 8\}$  being Gell-Mann matrices in colour space, expresses the diquarks' colour antitriplet character;  $C = \gamma_2\gamma_4$  is the charge-conjugation matrix; and  $\vec{t}_f = (t_f^1, t_f^2, t_f^3)$  are the flavour matrices:

$$t_f^1 = \frac{1}{2}(\tau^0 + \tau^3), \quad (\text{C.27a})$$

$$t_f^2 = \frac{1}{\sqrt{2}}\tau^1, \quad (\text{C.27b})$$

$$t_f^3 = \frac{1}{2}(\tau^0 - \tau^3). \quad (\text{C.27c})$$

The coupling constant,  $g_{1+}$ , is determined by the canonical normalisation condition:

$$2K_\mu = \frac{\partial}{\partial Q_\mu} \Pi(K; Q) \Big|_{Q=K}^{K^2=-m_{1+}^2}, \quad (\text{C.28a})$$

$$\Pi(K, Q) = \frac{1}{3} T_{\rho\nu}^K \Pi_{\rho\nu}(K; Q), \quad (\text{C.28b})$$

$$\begin{aligned} \Pi_{\rho\nu}(K, Q) &= \text{tr}_{\text{CDF}} \int \frac{d^4k}{(2\pi)^4} \bar{\Gamma}_\rho^{1+}(k; -K) \\ &\times S(k + Q/2) \Gamma_\nu^{1+}(k; K) S^T(-k + Q/2), \end{aligned} \quad (\text{C.28c})$$

where  $T_{\rho\nu}^K = [\delta_{\rho\nu} + K_\rho K_\nu / m_{1+}^2]$  and

$$\bar{\Gamma}_\mu^{1+}(k; K) = C^\dagger \Gamma_\mu^{1+}(-k; K) C. \quad (\text{C.29})$$

Using Eqs. (14), (C.26), and (C.28), one finds

$$g_{1+} = 12.7. \quad (\text{C.30})$$

In order to solve the Faddeev equation, Fig. 1, one also needs to specify the diquark propagator:

$$\mathcal{D}_{\mu\nu}^{1+}(K) = \left[ \delta_{\mu\nu} + \frac{K_\mu K_\nu}{m_{1+}^2} \right] \frac{1}{m_{1+}^2} \mathcal{F}(k^2/\omega_{1+}^2). \quad (\text{C.31})$$

## Appendix C.3: $\Delta$ Faddeev amplitude

The solution of the  $\Delta(1232)$ -baryon Faddeev equation, specified generically by Fig. 1, takes the form:

$$\Psi_{\mu\nu}^\Delta(\ell; P) = \sum_{k=1}^8 a_k^\Delta(\ell^2; \ell \cdot P) \mathcal{D}_{\mu\nu}^k(\ell; P) \frac{\lambda_c^0}{\sqrt{3}} \vec{s}_f, \quad (\text{C.32a})$$

$$\mathcal{D}_{\mu\nu}^k = \mathcal{S}^k \delta_{\mu\nu}, \quad k = 1, 2, \quad (\text{C.32b})$$

$$\mathcal{D}_{\mu\nu}^k = i\gamma_5 \mathcal{A}_\mu^{k-2} \ell_\nu^\perp, \quad k = 3, \dots, 8, \quad (\text{C.32c})$$

where

$$\mathcal{S}^1 = \mathbb{I}_D, \quad (\text{C.33a})$$

$$\mathcal{S}^2 = i\gamma \cdot \hat{\ell} - \hat{\ell} \cdot \hat{P} \mathbb{I}_D, \quad (\text{C.33b})$$

$$\mathcal{A}_\mu^1 = \gamma \cdot \ell^\perp \hat{P}_\mu, \quad (\text{C.33c})$$

$$\mathcal{A}_\mu^2 = -i\hat{P}_\mu \mathbb{I}_D, \quad (\text{C.33d})$$

$$\mathcal{A}_\mu^3 = \gamma \cdot \hat{\ell}^\perp \hat{\ell}_\mu^\perp, \quad (\text{C.33e})$$

$$\mathcal{A}_\mu^4 = i\hat{\ell}_\mu^\perp \mathbb{I}_D, \quad (\text{C.33f})$$

$$\mathcal{A}_\mu^5 = \gamma_\mu^\perp - \mathcal{A}_\mu^3, \quad (\text{C.33g})$$

$$\mathcal{A}_\mu^6 = i\gamma_\mu^\perp \gamma \cdot \hat{\ell}^\perp - \mathcal{A}_\mu^4, \quad (\text{C.33h})$$

are the Dirac basis matrices, with  $\hat{\ell}^2 = 1$ ,  $\hat{P}^2 = -1$ ,  $\ell_\nu^\perp = \hat{\ell}_\nu + \hat{\ell} \cdot \hat{P} \hat{P}_\nu$ ,  $\gamma_\nu^\perp = \gamma_\nu + \gamma \cdot \hat{P} \hat{P}_\nu$ ;  $\lambda_c^0 = \text{diag}[1, 1, 1]$  is a colour matrix; and  $\vec{s}_f$  are the flavour matrices of the quark+diquark amplitude, which are obtained by removing the diquark's flavour matrices (C.27) from the  $\Delta$ 's full amplitude,

$$s_f^1 = \begin{pmatrix} 1 & 0 & 0 & 0 \\ 0 & \sqrt{\frac{1}{3}} & 0 & 0 \end{pmatrix}, \quad (\text{C.34a})$$

$$s_f^2 = \begin{pmatrix} 0 & \sqrt{\frac{2}{3}} & 0 & 0 \\ 0 & 0 & \sqrt{\frac{2}{3}} & 0 \end{pmatrix}, \quad (\text{C.34b})$$

$$s_f^3 = \begin{pmatrix} 0 & 0 & \sqrt{\frac{1}{3}} & 0 \\ 0 & 0 & 0 & 1 \end{pmatrix}. \quad (\text{C.34c})$$

Upon solving the Faddeev equation, one obtains all scalar functions in Eq. (C.32) and the  $\Delta$ -baryon mass. Using Eq. (14),

$$m_\Delta = 1.35 \text{ GeV}. \quad (\text{C.35})$$

Notably, the kernel in Fig. 1 omits all those contributions which may be linked with meson-baryon final-state interactions, *i.e.*, the terms resummed in DCC models in order to transform a bare-baryon into the observed state [68, 81–83]. The Faddeev equation outputs should thus be viewed as describing the *dressed-quark core* of the  $\Delta$ -baryon, not the completely-dressed, observable object [84–86]. In support of this interpretation, we refer to Ref. [21, Fig. 4], which shows mass

predictions for the four lowest-lying  $\Delta$ -baryon multiplets. Evidently, by subtracting  $\delta_{\text{MB}} = 0.17 \text{ GeV}$  from each calculated mass, a value that matches the offset between bare and dressed  $\Delta(1232)_{\frac{3}{2}}^+$  masses determined in the DCC analysis of Ref. [82], one finds level orderings and splitting that match well with experiment.

## Appendix D: Current diagrams

In Fig. 2, we draw the symmetry preserving current appropriate to a baryon whose structure is prescribed by the Faddeev equation indicated by Fig. 1. In general there are six distinct sorts of terms. Diagrams (1) and (2) may be called impulse contributions: the probe strikes either a quark or a diquark. Diagram (3) is a partner to Diagram (2). In cases where more than one type of diquark correlation is present in the target baryon, then this contribution expresses probe-induced transitions between different types, *e.g.*, in the nucleon, it describes transitions between scalar and axialvector diquarks. Naturally, since there are only axialvector diquarks in  $\Delta$ -baryons, this diagram vanishes in the calculation of  $\Delta$ -baryon elastic form factors. That is why it is “red boxed” in Fig. 2. Impulse contributions are typically one-loop diagrams, *i.e.*, four dimensional integrals; and when that is the case, they can readily be evaluated using Gaussian quadrature methods.

The remaining contributions appear because the quark exchanged in the Faddeev equation kernel is also struck by the probe. Diagram (4) is the explicit interaction contribution. Diagrams (5), (6) are so-called seagull terms, whose presence guarantees that all Ward-Green-Takahashi identities associated with the interaction probe are preserved at the baryon level. The seagulls for electromagnetic interactions were derived in Ref. [87] and those for weak interactions in Ref. [15]. These three contributions are two-loop diagrams, which we evaluate using Monte-Carlo methods.

For explicit calculations, we use the Breit frame:  $P_i = K - Q/2$ ,  $P_f = K + Q/2$ ,  $K = (0, 0, 0, iE_\Delta(Q))$ ,  $E_\Delta^2(Q) = m_\Delta^2 + Q^2/4$ .

### Appendix D.1: Diagram (1)

Probe coupling directly to the uncorrelated quark:

$$J_{5(\mu),\lambda\omega}^q(K, Q) = \int_{dp} \bar{\Psi}_{\lambda\alpha}^\Delta(p'_f; -P_f) S(p_{q_+}) \times \Gamma_{5(\mu)}^j(p_{q_+}, p_{q_-}) S(p_{q_-}) \mathcal{D}_{\alpha\beta}^{1+}(p_d) \Psi_{\beta\omega}^\Delta(p'_i; P_i), \quad (\text{D.36})$$

where  $\Gamma_{5(\mu)}^j$  is the dressed-quark pseudoscalar (axialvector) vertex,

$$p'_i = p - \hat{\eta}Q/2, \quad p'_f = p + \hat{\eta}Q/2, \quad (\text{D.37a})$$

$$p_{q_-} = p'_i + \eta P_i, \quad p_{q_+} = p'_f + \eta P_f, \quad (\text{D.37b})$$

$$p_d = \hat{\eta}P_i - p'_i = \hat{\eta}P_f - p'_f.$$

The dressed-quark axialvector and pseudoscalar vertices satisfy the axialvector Ward-Green-Takahashi identity (AWGTI):

$$Q_\mu \Gamma_{5\mu}^j(k_+, k_-) + 2im_q \Gamma_5^j(k_+, k_-) = S^{-1}(k_+) i\gamma_5 \frac{\tau^j}{2} + \frac{\tau^j}{2} i\gamma_5 S^{-1}(k_-), \quad (\text{D.38})$$

where  $Q$  is the incoming probe momentum,  $k_-$ ,  $k_+$  are the incoming and outgoing quark momenta,  $k_\pm = k \pm Q/2$ . Preserving the AWGTI is crucial for PCAC [15] and the following forms ensure this outcome:

$$\Gamma_{5\mu}^j(k_+, k_-) = \frac{\tau^j}{2} \gamma_5 \left[ \gamma_\mu \Sigma_A^{+-} + 2\gamma \cdot k k_\mu \Delta_A^{+-} + 2i \frac{Q_\mu}{Q^2 + m_\pi^2} \Sigma_B^{+-} \right], \quad (\text{D.39a})$$

$$i\Gamma_5^j(k_+, k_-) = \frac{\tau^j}{2} \frac{m_\pi^2}{Q^2 + m_\pi^2} \frac{1}{m_q} i\gamma_5 \Sigma_B^{+-}, \quad (\text{D.39b})$$

where

$$\Sigma_F^{+-} = \frac{1}{2} [F(k_+^2) + F(k_-^2)], \quad (\text{D.40a})$$

$$\Delta_F^{+-} = \frac{F(k_+^2) - F(k_-^2)}{k_+^2 - k_-^2}, \quad (\text{D.40b})$$

with  $F \in \{A, B\}$  and  $A$  and  $B$  are the dressing functions in the quark propagator – see Eq. (C.21b) in Appendix C.1.

### Appendix D.2: Diagram (2)

Probe coupling to an axialvector diquark:

$$J_{5(\mu),\lambda\omega}^{\text{dq}}(K, Q) = \int_{dp} \bar{\Psi}_{\lambda\alpha}^\Delta(p'_f; -P_f) \mathcal{D}_{\alpha\rho}^{1+}(p_{d_+}) \times \Gamma_{5(\mu),\rho\sigma}^{AA}(p_{d_+}, p_{d_-}) \mathcal{D}_{\sigma\beta}^{1+}(p_{d_-}) \times S(p_q) \Psi_{\beta\omega}^\Delta(p'_i; P_i), \quad (\text{D.41})$$

where  $\Gamma_{5(\mu),\rho\sigma}^{AA}$  is the axialvector diquark pseudoscalar (axialvector) vertex and

$$p''_i = p + \eta Q/2, \quad p''_f = p - \eta Q/2, \quad (\text{D.42a})$$

$$p_{d_-} = \hat{\eta}P_i - p''_i, \quad p_{d_+} = \hat{\eta}P_f - p''_f, \quad (\text{D.42b})$$

$$p_q = p''_i + \eta P_i = p''_f + \eta P_f.$$

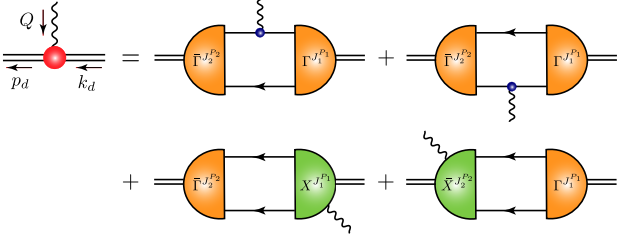


**Fig. 9** Interaction vertex for the  $J_1^{P_1} \rightarrow J_2^{P_2}$  diquark transition ( $p_d = k_d + Q$ ): *single line*, quark propagator; *undulating line*, the axial or pseudoscalar current;  $\Gamma$ , diquark correlation amplitude; *double line*, diquark propagator; and  $\chi$ , seagull interaction. For  $\Gamma_{5(\mu),\rho\sigma}^{AA}$  in Eq. (D.41),  $J_1^{P_1} = J_2^{P_2} = 1^+$ .

Each current-diquark vertex receives four contributions, *viz.* those depicted in Fig. 9. Two of them are generated by coupling the current to the upper and lower quark lines of the resolved diquark. The remaining two are current couplings to the diquark amplitudes, *i.e.*, “seagull terms” – see Appendix D.4 for details. Consequently,  $\Gamma_{5(\mu),\rho\sigma}^{AA}$  can be expressed as the following one-loop integral:

$$\begin{aligned} & \Gamma_{5(\mu),\rho\sigma}^{AA}(p_d, k_d) = \\ & -\text{tr}_D \int_{d\ell} \left[ \bar{\Gamma}_\rho^{1+}(\ell_r) S(\ell_2) \Gamma_{5(\mu)}^j(\ell_2, \ell_1) S(\ell_1) \Gamma_\sigma^{1+}(\ell'_r) S^T(\ell_3) \right. \\ & + \bar{\Gamma}_\rho^{1+}(\tilde{\ell}_r) S(\tilde{\ell}_3) \Gamma_\sigma^{1+}(\tilde{\ell}'_r) [S(\tilde{\ell}_2) \Gamma_{5(\mu)}^j(\tilde{\ell}_2, \tilde{\ell}_1) S(\tilde{\ell}_1)]^T \\ & + \bar{\Gamma}_\rho^{1+}(\ell) S(\ell_+) \chi_{5(\mu),\sigma}^{1+}(\ell, Q) S^T(-\ell_-) \\ & \left. + \bar{\chi}_{5(\mu),\rho}^{1+}(\ell, Q) S(\tilde{\ell}_+) \Gamma_\sigma^{1+}(\ell) S^T(-\tilde{\ell}_-) \right], \end{aligned} \quad (\text{D.43})$$

with

$$\ell_{\frac{1}{2}} = \frac{p_d + k_d}{4} \mp \frac{Q}{2} + \ell, \quad (\text{D.44a})$$

$$\ell_3 = \frac{p_d + k_d}{4} - \ell, \quad (\text{D.44b})$$

$$\ell_r = \frac{\ell_2 - \ell_3}{2}, \ell'_r = \frac{\ell_1 - \ell_3}{2}, \quad (\text{D.44c})$$

$$\tilde{\ell}_{\frac{1}{2}} = \frac{p_d + k_d}{4} \mp \frac{Q}{2} - \ell, \quad (\text{D.44d})$$

$$\tilde{\ell}_3 = \frac{p_d + k_d}{4} + \ell, \quad (\text{D.44e})$$

$$\tilde{\ell}_r = \frac{\tilde{\ell}_2 - \tilde{\ell}_3}{2}, \tilde{\ell}'_r = \frac{\tilde{\ell}_1 - \tilde{\ell}_3}{2}, \quad (\text{D.44f})$$

$$\ell_{\pm} = \frac{p_d}{2} \pm \ell, \tilde{\ell}_{\pm} = \frac{k_d}{2} \pm \ell. \quad (\text{D.44g})$$

Inserting Eq. (D.43) into Eq. (D.41), it becomes clear that Diagram (2) is, herein, a two-loop diagram, and its computation requires Monte-Carlo methods.

Notably, for nucleon axial form factors, Refs. [14–16] constructed *Ansätze* for the current-diquark vertices,

ensuring that Diagram (2) remained a 1-loop integral. This approach cannot efficiently be employed herein because the  $\Delta$ -baryon has two independent sets of axialvector and pseudoscalar form factors, *viz.*  $\{g_1, g_3, \tilde{g}\}$  and  $\{h_1, h_3, \tilde{h}\}$ .

### Appendix D.3: Diagram (4)

Probe coupling to the quark exchanged as one diquark breaks-up and another is formed:

$$\begin{aligned} & J_{5(\mu),\lambda\omega}^{\text{ex}}(K, Q) = \int_{dp} \int_{dk} \bar{\Psi}_{\lambda\rho}^\Delta(p; -P_f) \mathcal{D}_{\rho\alpha}^{1+}(\tilde{p}_{d+}) \\ & \times S(\tilde{p}_{q+}) \Gamma_\alpha^{1+}(\tilde{k}_r) [S(\tilde{q}') \Gamma_{5(\mu)}^j(\tilde{q}', \tilde{q}) S(\tilde{q})]^T \bar{\Gamma}_\beta^{1+}(\tilde{p}'_r) \\ & \times S(\tilde{p}_{q-}) \mathcal{D}_{\beta\sigma}^{1+}(\tilde{p}_{d-}) \Psi_{\sigma\omega}^\Delta(k; P_i), \end{aligned} \quad (\text{D.45})$$

with

$$\tilde{p}_{q-} = k + \eta P_i, \tilde{p}_{q+} = p + \eta P_f, \quad (\text{D.46a})$$

$$\tilde{p}_{d-} = \hat{\eta} P_i - k, \tilde{p}_{d+} = \hat{\eta} P_f - p, \quad (\text{D.46b})$$

$$\tilde{k}_r = \frac{1}{2}((k + \hat{\eta} Q) + 2p + (3\eta - 1)P_f), \quad (\text{D.46c})$$

$$\tilde{p}_r = \frac{1}{2}(p + 2(k + \hat{\eta} Q) + (3\eta - 1)P_f), \quad (\text{D.46d})$$

$$\tilde{q} = -p - (k + \hat{\eta} Q) + (1 - 2\eta)P_f, \quad (\text{D.46e})$$

$$\tilde{k}'_r = \tilde{k}_r - Q, \tilde{p}'_r = \tilde{p}_r - Q, \tilde{q}' = \tilde{q} + Q. \quad (\text{D.46f})$$

The process of quark exchange in their Faddeev kernel provides the attraction required to bind the  $\Delta$ -baryon. It also ensures that the Faddeev amplitude has the correct antisymmetry under the exchange of any two dressed quarks. These features are absent in models with pointlike diquarks.

### Appendix D.4: Diagrams (5) and (6)

Owing to the nonpointlike character of the diquark correlations, one must also consider couplings of the incoming probe to the diquark amplitudes, *viz.* “seagull terms”, which appear as partners to Diagram (4) and are necessary to ensure current conservation [87]. The seagull terms for the axialvector and pseudoscalar currents are derived in Ref. [15]. One has

$$\begin{aligned} & J_{5(\mu),\lambda\omega}^{\text{sg}}(K, Q) = \int_{dp} \int_{dk} \bar{\Psi}_{\lambda\rho}^\Delta(p; -P_f) \mathcal{D}_{\rho\alpha}^{1+}(\tilde{p}_{d+}) \\ & \times S(\tilde{p}_{q+}) \chi_{5(\mu),\alpha}^{j,1+}(k_1, Q) S^T(\tilde{q}') \bar{\Gamma}_\beta^{1+}(\tilde{p}'_r) S(\tilde{p}_{q-}) \\ & \times \mathcal{D}_{\beta\sigma}^{1+}(\tilde{p}_{d-}) \Psi_{\sigma\omega}^\Delta(k; P_i), \end{aligned} \quad (\text{D.47})$$

for Diagram (5), and

$$J_{5(\mu),\lambda\omega}^{\text{sg}}(K, Q) = \int_{dp} \int_{dk} \bar{\Psi}_{\lambda\rho}^\Delta(p; -P_f) \mathcal{D}_{\rho\alpha}^{1+}(\tilde{p}_{d+})$$

$$\begin{aligned} & \times S(\tilde{p}_{q+})\Gamma_\alpha^{1+}(\tilde{k}_r)S^T(\tilde{q})\bar{\chi}_{5(\mu),\beta}^{j,1+}(k_2, Q)S(\tilde{p}_{q-}) \\ & \times \mathcal{D}_{\beta\sigma}^{1+}(\tilde{p}_{d-})\Psi_{\sigma\omega}^\Delta(k; P_i), \end{aligned} \quad (\text{D.48})$$

for Diagram (6). The momenta are

$$k_1 = \frac{\tilde{p}_{q+} - \tilde{q}'}{2}, \quad k_2 = \frac{\tilde{p}_{q-} - \tilde{q}}{2}. \quad (\text{D.49})$$

Explicitly, the seagull terms are:

$$\begin{aligned} \chi_{5\mu,\alpha}^{j,1+}(k, Q) = & -\frac{Q_\mu}{Q^2 + m_\pi^2} \left[ \frac{\tau^j}{2} i\gamma_5 \Gamma_\alpha^{1+}(k - Q/2) + \right. \\ & \left. \Gamma_\alpha^{1+}(k + Q/2) (i\gamma_5 \frac{\tau^j}{2})^T \right], \end{aligned} \quad (\text{D.50a})$$

$$\begin{aligned} i\chi_{5,\alpha}^{j,1+}(k, Q) = & -\frac{1}{2m_q} \frac{m_\pi^2}{Q^2 + m_\pi^2} \left[ \frac{\tau^j}{2} i\gamma_5 \Gamma_\alpha^{1+}(k - Q/2) + \right. \\ & \left. \Gamma_\alpha^{1+}(k + Q/2) (i\gamma_5 \frac{\tau^j}{2})^T \right], \end{aligned} \quad (\text{D.50b})$$

$$\begin{aligned} \bar{\chi}_{5\mu,\alpha}^{j,1+}(k, Q) = & -\frac{Q_\mu}{Q^2 + m_\pi^2} \left[ \bar{\Gamma}_\alpha^{1+}(k + Q/2) \frac{\tau^j}{2} i\gamma_5 + \right. \\ & \left. (i\gamma_5 \frac{\tau^j}{2})^T \bar{\Gamma}_\alpha^{1+}(k - Q/2) \right], \end{aligned} \quad (\text{D.50c})$$

$$\begin{aligned} i\bar{\chi}_{5,\alpha}^{j,1+}(k, Q) = & -\frac{1}{2m_q} \frac{m_\pi^2}{Q^2 + m_\pi^2} \left[ \bar{\Gamma}_\alpha^{1+}(k + Q/2) \frac{\tau^j}{2} i\gamma_5 + \right. \\ & \left. (i\gamma_5 \frac{\tau^j}{2})^T \bar{\Gamma}_\alpha^{1+}(k - Q/2) \right]. \end{aligned} \quad (\text{D.50d})$$

The axialvector and pseudoscalar seagull terms are related by the following AWGTI:

$$\begin{aligned} & Q_\mu \chi_{5\mu,\alpha}^{j,1+}(k, Q) + 2im_q \chi_{5,\alpha}^{j,1+}(k, Q) \\ = & -\frac{\tau^j}{2} i\gamma_5 \Gamma_\alpha^{1+}(k - Q/2) - \Gamma_\alpha^{1+}(k + Q/2) (i\gamma_5 \frac{\tau^j}{2})^T. \end{aligned} \quad (\text{D.51})$$

Using Eqs. (D.38), (D.51), it is straightforward to obtain the AWGTI for the axialvector diquark vertices, Eq. (D.43):

$$Q_\mu \Gamma_{5\mu,\rho\sigma}^{AA}(p_d, k_d) + 2im_q \Gamma_{5,\rho\sigma}^{AA}(p_d, k_d) = 0. \quad (\text{D.52})$$

## Appendix E: Interpolation of the form factors

For  $-m_\pi^2 < s = Q^2 < 1.6m_\Delta^2$ , the  $\Delta$ -baryon axialvector and  $\pi$ - $\Delta$  form factors can accurately be interpolated using the following function:

$$\frac{a_0 + a_1 s}{1 + b_1 s + b_2 s^2}, \quad (\text{E.53})$$

for  $g_1$ ,  $h_1$ ,  $G_{\pi\Delta\Delta}$  and  $H_{\pi\Delta\Delta}$ ; and

$$\frac{a_0 + a_1 s}{1 + b_1 s + b_2 s^2} \mathcal{R}(s), \quad (\text{E.54})$$

**Table 2** Interpolation parameters for  $\Delta$ -baryon's axialvector and  $\pi$ - $\Delta$  form factors, Eqs.(E.53) and (E.54).

	$a_0$	$a_1$	$b_1$	$b_2$
$g_1$	0.71	0.024	1.25	0.56
$g_3$	1.00	0.046	1.23	0.60
$h_1$	2.40	-0.32	1.30	0.52
$h_3$	3.43	-0.47	1.31	0.52
$G_{\pi\Delta\Delta}$	10.16	-2.55	1.29	1.14
$H_{\pi\Delta\Delta}$	34.50	-7.64	1.62	1.22

for  $g_3$  and  $h_3$ , where

$$\mathcal{R}(s) = \frac{m_\pi^2}{s + m_\pi^2} \frac{m_\Delta}{f_\pi}. \quad (\text{E.55})$$

The coefficients for the central results are listed in Table 2.

## References

1. R. J. Holt, C. D. Roberts, Distribution Functions of the Nucleon and Pion in the Valence Region, Rev. Mod. Phys. 82 (2010) 2991–3044.
2. R. Holt, R. Gilman, Transition between nuclear and quark-gluon descriptions of hadrons and light nuclei, Rept. Prog. Phys. 75 (2012) 086301.
3. V. Punjabi, C. F. Perdrisat, M. K. Jones, E. J. Brash, C. E. Carlson, The Structure of the Nucleon: Elastic Electromagnetic Form Factors, Eur. Phys. J. A 51 (2015) 79.
4. S. J. Brodsky, A. L. Deshpande, H. Gao, R. D. McKeown, C. A. Meyer, Z.-E. Meziani, R. G. Milner, J. Qiu, D. G. Richards, C. D. Roberts, QCD and Hadron Physics – arXiv:1502.05728 [hep-ph].
5. D. Carman, K. Joo, V. Mokeev, Strong QCD Insights from Excited Nucleon Structure Studies with CLAS and CLAS12, Few Body Syst. 61 (2020) 29.
6. D. P. Anderle, et al., Electron-ion collider in China, Front. Phys. (Beijing) 16 (6) (2021) 64701.
7. R. Abdul Khalek, et al., Science Requirements and Detector Concepts for the Electron-Ion Collider: EIC Yellow Report, Nucl. Phys. A 1026 (2022) 122447.
8. C. Quintans, The New AMBER Experiment at the CERN SPS, Few Body Syst. 63 (4) (2022) 72.
9. D. S. Carman, R. W. Gothe, V. I. Mokeev, C. D. Roberts, Nucleon Resonance Electroexcitation Amplitudes and Emergent Hadron Mass, Particles 6 (1) (2023) 416–439.
10. G. Eichmann, H. Sanchis-Alepuz, R. Williams, R. Alkofer, C. S. Fischer, Baryons as relativistic three-quark bound states, Prog. Part. Nucl. Phys. 91 (2016) 1–100.
11. S. J. Brodsky, et al., Strong QCD from Hadron Structure Experiments, Int. J. Mod. Phys. E 29 (08) (2020) 2030006.
12. M. Ding, C. D. Roberts, S. M. Schmidt, Emergence of Hadron Mass and Structure, Particles 6 (1) (2023) 57–120.
13. I. V. Anikin, V. M. Braun, N. Offen, Axial form factor of the nucleon at large momentum transfers, Phys. Rev. D 94 (3) (2016) 034011.

14. C. Chen, C. S. Fischer, C. D. Roberts, J. Segovia, Form Factors of the Nucleon Axial Current, *Phys. Lett. B* 815 (2021) 136150.
15. C. Chen, C. S. Fischer, C. D. Roberts, J. Segovia, Nucleon axial-vector and pseudoscalar form factors and PCAC relations, *Phys. Rev. D* 105 (9) (2022) 094022.
16. C. Chen, C. D. Roberts, Nucleon axial form factor at large momentum transfers, *Eur. Phys. J. A* 58 (2022) 206.
17. C. Alexandrou, M. Constantinou, K. Hadjiyiannakou, K. Jansen, C. Kallidonis, G. Koutsou, A. Vaquero Aviles-Casco, Nucleon axial form factors using  $N_f = 2$  twisted mass fermions with a physical value of the pion mass, *Phys. Rev. D* 96 (2017) 054507.
18. Y.-C. Jang, R. Gupta, B. Yoon, T. Bhattacharya, Axial Vector Form Factors from Lattice QCD that Satisfy the PCAC Relation, *Phys. Rev. Lett.* 124 (2020) 072002.
19. G. S. Bali, L. Barca, S. Collins, M. Gruber, M. Löffler, A. Schäfer, W. Söldner, P. Wein, S. Weishäupl, T. Wurm, Nucleon axial structure from lattice QCD, *JHEP* 05 (2020) 126 (2020).
20. M. Y. Barabanov, et al., Diquark Correlations in Hadron Physics: Origin, Impact and Evidence, *Prog. Part. Nucl. Phys.* 116 (2021) 103835.
21. L. Liu, C. Chen, Y. Lu, C. D. Roberts, J. Segovia, Composition of low-lying  $J = \frac{3}{2}^\pm$   $\Delta$ -baryons, *Phys. Rev. D* 105 (11) (2022) 114047.
22. C. Alexandrou, T. Korzec, T. Leontiou, J. W. Negele, A. Tsapalis, Electromagnetic form-factors of the  $\Delta$  baryon, *PoS LAT2007* (2007) 149.
23. C. Alexandrou, T. Korzec, G. Koutsou, C. Lorce, J. W. Negele, et al., Quark transverse charge densities in the  $\Delta(1232)$  from lattice QCD, *Nucl. Phys. A* 825 (2009) 115–144.
24. D. Nicmorus, G. Eichmann, R. Alkofer, Delta and Omega electromagnetic form factors in a Dyson-Schwinger/Bethe-Salpeter approach, *Phys. Rev. D* 82 (2010) 114017.
25. T. Ledwig, J. Martin-Camalich, V. Pascalutsa, M. Vanderhaeghen, The Nucleon and  $\Delta(1232)$  form factors at low momentum-transfer and small pion masses, *Phys. Rev. D* 85 (2012) 034013.
26. C. Alexandrou, C. Papanicolas, M. Vanderhaeghen, The Shape of Hadrons, *Rev. Mod. Phys.* 84 (2012) 1231.
27. J. Segovia, C. Chen, I. C. Cloet, C. D. Roberts, S. M. Schmidt, S.-L. Wan, Elastic and transition form factors of the  $\Delta(1232)$ , *Few Body Syst.* 55 (2014) 1–33.
28. J. Segovia, I. C. Cloet, C. D. Roberts, S. M. Schmidt, Nucleon and  $\Delta$  elastic and transition form factors, *Few Body Syst.* 55 (2014) 1185–1222.
29. J.-Y. Kim, H.-C. Kim, Electromagnetic form factors of the baryon decuplet with flavor SU(3) symmetry breaking, *Eur. Phys. J. C* 79 (7) (2019) 570.
30. R. L. Workman, et al., Review of Particle Physics, *PTEP* 2022 (2022) 083C01.
31. S.-Z. Jiang, Y.-R. Liu, H.-Q. Wang, Q.-H. Yang, Chiral Lagrangians with decuplet baryons to one loop, *Phys. Rev. D* 97 (5) (2018) 054031.
32. M. Holmberg, S. Leupold, The relativistic chiral Lagrangian for decuplet and octet baryons at next-to-leading order, *Eur. Phys. J. A* 54 (6) (2018) 103.
33. U. Mosel, Neutrino Interactions with Nucleons and Nuclei: Importance for Long-Baseline Experiments, *Ann. Rev. Nucl. Part. Sci.* 66 (2016) 171–195.
34. L. Alvarez-Ruso, et al., NuSTEC White Paper: Status and challenges of neutrino–nucleus scattering, *Prog. Part. Nucl. Phys.* 100 (2018) 1–68.
35. A. Lovato, J. Carlson, S. Gandolfi, N. Rocco, R. Schiavilla, Ab initio study of  $(\nu_\ell, \ell^-)$  and  $(\bar{\nu}_\ell, \ell^+)$  inclusive scattering in  $^{12}\text{C}$ : confronting the MiniBooNE and T2K CCQE data, *Phys. Rev. X* 10 (2020) 031068.
36. D. Simons, N. Steinberg, A. Lovato, Y. Meurice, N. Rocco, M. Wagman, Form factor and model dependence in neutrino-nucleus cross section predictions – arXiv:2210.02455 [hep-ph] .
37. G. E. Brown, W. Weise, Pion Scattering and Isobars in Nuclei, *Phys. Rept.* 22 (1975) 279–337.
38. R. F. Dashen, E. E. Jenkins, A. V. Manohar, The  $1/N(c)$  expansion for baryons, *Phys. Rev. D* 49 (1994) 4713, [Erratum: *Phys. Rev. D* 51, 2489 (1995)].
39. S.-L. Zhu,  $\pi\Delta\Delta$  coupling constant, *Phys. Rev. C* 63 (2001) 018201.
40. C. Alexandrou, E. B. Gregory, T. Korzec, G. Koutsou, J. W. Negele, T. Sato, A. Tsapalis, The  $\Delta(1232)$  axial charge and form factors from lattice QCD, *Phys. Rev. Lett.* 107 (2011) 141601.
41. C. Alexandrou, E. B. Gregory, T. Korzec, G. Koutsou, J. W. Negele, T. Sato, A. Tsapalis, Determination of the  $\Delta(1232)$  axial and pseudoscalar form factors from lattice QCD, *Phys. Rev. D* 87 (11) (2013) 114513.
42. C. Alexandrou, K. Hadjiyiannakou, C. Kallidonis, Axial charges of hyperons and charmed baryons using  $N_f = 2 + 1 + 1$  twisted mass fermions, *Phys. Rev. D* 94 (3) (2016) 034502.
43. F.-J. Jiang, B. C. Tiburzi, Chiral Corrections and the Axial Charge of the Delta, *Phys. Rev. D* 78 (2008) 017504.
44. K.-S. Choi, W. Plessas, R. F. Wagenbrunn, Axial charges of octet and decuplet baryons, *Phys. Rev. D* 82 (2010) 014007.
45. A. J. Buchmann, S. A. Moszkowski, Pion couplings of the  $\Delta(1232)$ , *Phys. Rev. C* 87 (2) (2013) 028203.
46. A. Kucukarslan, U. Ozdem, A. Ozpineci, Isovector axial vector and pseudoscalar transition form factors of  $\Delta$  in QCD, *Phys. Rev. D* 90 (2014) 054002.
47. Z. Wang, B.-Q. Ma, A unified approach to hadron phenomenology at zero and finite temperatures in a hard-wall AdS/QCD model, *Eur. Phys. J. A* 52 (5) (2016) 122.
48. D.-L. Yao, D. Siemens, V. Bernard, E. Epelbaum, A. M. Gasparyan, J. Gegelia, H. Krebs, U.-G. Meißner, Pion-nucleon scattering in covariant baryon chiral perturbation theory with explicit Delta resonances, *JHEP* 05 (2016) 038.
49. X. Y. Liu, D. Samart, K. Khosonthongkee, A. Limphirat, K. Xu, Y. Yan, Axial charges of octet and decuplet baryons in a perturbative chiral quark model, *Phys. Rev. C* 97 (5) (2018) 055206.
50. Y.-S. Jun, J.-M. Suh, H.-C. Kim, Axial-vector form factors of the baryon decuplet with flavor SU(3) symmetry breaking, *Phys. Rev. D* 102 (5) (2020) 054011.
51. C. S. Fischer, QCD at finite temperature and chemical potential from Dyson–Schwinger equations, *Prog. Part. Nucl. Phys.* 105 (2019) 1–60.
52. S.-X. Qin, C. D. Roberts, Impressions of the Continuum Bound State Problem in QCD, *Chin. Phys. Lett.* 37 (12) (2020) 121201.
53. D. Binosi, Emergent Hadron Mass in Strong Dynamics, *Few Body Syst.* 63 (2) (2022) 42.
54. J. Papavassiliou, Emergence of mass in the gauge sector of QCD, *Chin. Phys. C* 46 (11) (2022) 112001.
55. M. N. Ferreira, J. Papavassiliou, Gauge Sector Dynamics in QCD, *Particles* 6 (1) (2023) 312–363.



56. R. T. Cahill, C. D. Roberts, J. Praschifka, Baryon structure and QCD, *Austral. J. Phys.* 42 (1989) 129–145.
57. H. Reinhardt, Hadronization of Quark Flavor Dynamics, *Phys. Lett. B* 244 (1990) 316–326.
58. G. V. Efimov, M. A. Ivanov, V. E. Lyubovitskij, Quark - diquark approximation of the three quark structure of baryons in the quark confinement model, *Z. Phys. C* 47 (1990) 583–594.
59. E. L. Isupov, et al., Measurements of  $ep \rightarrow e'\pi^+\pi^-p'$  Cross Sections with CLAS at  $1.40 \text{ GeV} < W < 2.0 \text{ GeV}$  and  $2.0 \text{ GeV}^2 < Q^2 < 5.0 \text{ GeV}^2$ , *Phys. Rev. C* 96 (2) (2017) 025209.
60. G. V. Fedotov, et al., Measurements of the  $\gamma_v p \rightarrow p'\pi^+\pi^-$  cross section with the CLAS detector for  $0.4 \text{ GeV}^2 < Q^2 < 1.0 \text{ GeV}^2$  and  $1.3 \text{ GeV} < W < 1.825 \text{ GeV}$ , *Phys. Rev. C* 98 (2) (2018) 025203.
61. V. I. Mokeev, V. D. Burkert, T.-S. H. Lee, L. Elouadrhiri, G. V. Fedotov, B. S. Ishkhanov, Model Analysis of the  $p\pi^+\pi^-$  Electroproduction Reaction on the Proton, *Phys. Rev. C* 80 (2009) 045212.
62. G. Eichmann, C. S. Fischer, Nucleon axial and pseudoscalar form factors from the covariant Faddeev equation, *Eur. Phys. J. A* 48 (2012) 9.
63. V. D. Burkert, C. D. Roberts, Roper resonance: Toward a solution to the fifty-year puzzle, *Rev. Mod. Phys.* 91 (2019) 011003.
64. C. Chen, Y. Lu, D. Binosi, C. D. Roberts, J. Rodríguez-Quintero, J. Segovia, Nucleon-to-Roper electromagnetic transition form factors at large  $Q^2$ , *Phys. Rev. D* 99 (2019) 034013.
65. C. Chen, G. I. Krein, C. D. Roberts, S. M. Schmidt, J. Segovia, Spectrum and structure of octet and decuplet baryons and their positive-parity excitations, *Phys. Rev. D* 100 (2019) 054009.
66. Y. Lu, C. Chen, Z.-F. Cui, C. D. Roberts, S. M. Schmidt, J. Segovia, H. S. Zong, Transition form factors:  $\gamma^* + p \rightarrow \Delta(1232)$ ,  $\Delta(1600)$ , *Phys. Rev. D* 100 (2019) 034001.
67. Z.-F. Cui, C. Chen, D. Binosi, F. de Soto, C. D. Roberts, J. Rodríguez-Quintero, S. M. Schmidt, J. Segovia, Nucleon elastic form factors at accessible large spacelike momenta, *Phys. Rev. D* 102 (2020) 014043.
68. H. Kamano, S. X. Nakamura, T. S. H. Lee, T. Sato, Nucleon resonances within a dynamical coupled-channels model of  $\pi N$  and  $\gamma N$  reactions, *Phys. Rev. C* 88 (2013) 035209.
69. R. A. Arndt, J. B. Cammarata, Y. N. Goradia, R. H. Hackman, V. L. Teplitz, D. A. Dicus, R. Aaron, R. S. Longacre, Isobar Production in  $\pi^- p \rightarrow \pi^+\pi^-n$  Near Threshold, *Phys. Rev. D* 20 (1979) 651.
70. P. Cheng, Y. Yu, H.-Y. Xing, C. Chen, Z.-F. Cui, C. D. Roberts, Polarised parton distribution functions and proton spin – arXiv:2304.12469 [hep-ph] .
71. A. Deur, S. J. Brodsky, G. F. De Tera mond, The Spin Structure of the Nucleon, *Rept. Prog. Phys.* 82 (076201).
72. G. Eichmann, R. Alkofer, A. Krassnigg, D. Nicmorus, Nucleon mass from a covariant three-quark Faddeev equation, *Phys. Rev. Lett.* 104 (2010) 201601.
73. Q.-W. Wang, S.-X. Qin, C. D. Roberts, S. M. Schmidt, Proton tensor charges from a Poincaré-covariant Faddeev equation, *Phys. Rev. D* 98 (2018) 054019.
74. M. A. Ivanov, Yu. L. Kalinovsky, C. D. Roberts, Survey of heavy-meson observables, *Phys. Rev. D* 60 (1999) 034018.
75. M. B. Hecht, C. D. Roberts, S. M. Schmidt, Valence-quark distributions in the pion, *Phys. Rev. C* 63 (2001) 025213.
76. R. Alkofer, A. Höll, M. Kloker, A. Krassnigg, C. D. Roberts, On nucleon electromagnetic form-factors, *Few Body Syst.* 37 (2005) 1–31.
77. K. D. Lane, Asymptotic Freedom and Goldstone Realization of Chiral Symmetry, *Phys. Rev. D* 10 (1974) 2605.
78. H. D. Politzer, Effective Quark Masses in the Chiral Limit, *Nucl. Phys. B* 117 (1976) 397.
79. D. Binosi, L. Chang, J. Papavassiliou, S.-X. Qin, C. D. Roberts, Natural constraints on the gluon-quark vertex, *Phys. Rev. D* 95 (2017) 031501(R).
80. C. J. Burden, C. D. Roberts, M. J. Thomson, Electromagnetic Form Factors of Charged and Neutral Kaons, *Phys. Lett. B* 371 (1996) 163–168.
81. B. Julia-Diaz, T. S. H. Lee, A. Matsuyama, T. Sato, Dynamical coupled-channel model of  $\pi N$  scattering in the  $W \leq 2\text{-GeV}$  nucleon resonance region, *Phys. Rev. C* 76 (2007) 065201.
82. N. Suzuki, B. Julia-Diaz, H. Kamano, T. S. H. Lee, A. Matsuyama, T. Sato, Disentangling the Dynamical Origin of P-11 Nucleon Resonances, *Phys. Rev. Lett.* 104 (2010) 042302.
83. D. Rönchen, M. Döring, F. Huang, H. Haberzettl, J. Haidenbauer, C. Hanhart, S. Krewald, U. G. Meissner, K. Nakayama, Coupled-channel dynamics in the reactions  $\pi N \rightarrow \pi N, \eta N, K\Lambda, K\Sigma$ , *Eur. Phys. J. A* 49 (2013) 44.
84. G. Eichmann, R. Alkofer, I. C. Cloet, A. Krassnigg, C. D. Roberts, Perspective on rainbow-ladder truncation, *Phys. Rev. C* 77 (2008) 042202(R).
85. G. Eichmann, I. C. Cloet, R. Alkofer, A. Krassnigg, C. D. Roberts, Toward unifying the description of meson and baryon properties, *Phys. Rev. C* 79 (2009) 012202(R).
86. H. L. L. Roberts, L. Chang, I. C. Cloet, C. D. Roberts, Masses of ground and excited-state hadrons, *Few Body Syst.* 51 (2011) 1–25.
87. M. Oettel, M. Pichowsky, L. von Smekal, Current conservation in the covariant quark-diquark model of the nucleon, *Eur. Phys. J. A* 8 (2000) 251–281.